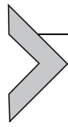

CHAPTER TWELVE

Electrical transport properties of hexagonal boron nitride epilayers

Samuel Grenadier, Avisek Maity, Jing Li, Jingyu Lin*, and Hongxing Jiang*

Department of Electrical and Computer Engineering, Texas Tech University, Lubbock, TX, United States
*Corresponding authors: e-mail address: jingyu.lin@ttu.edu; hx.jiang@ttu.edu

Contents

1. Introduction 394
2. Prospects of n- and p-type doping of h-BN 400
  2.1 Mg doping 400
  2.2 Si doping 404
  2.3 Carbon doping 405
3. Criteria of h-BN as thermal neutron detector materials 409
  3.1 Thickness requirement 410
  3.2 Requirements in background carrier concentration and dark electrical resistivity 413
  3.3 Necessary conditions for attaining high charge collection efficiencies 417
4. Vertical electrical transport properties and parameters 420
  4.1 Carrier mobility-lifetime product and surface recombination field characterization 420
  4.2 Charge collection efficiency characterization 424
  4.3 Thermal neutron detection efficiency characterization 426
5. Lateral electrical transport properties and parameters 430
  5.1 Lateral charge carrier transport properties probed by time-of-flight technique 430
  5.2 Attainment of 1 cm^2 h-^{10}BN lateral neutron detectors with unprecedented efficiency 435
  5.3 Characterizing transport parameters under thermal neutron irradiation 439
6. Dominant native and point defects in h-BN 440
  6.1 Oxygen impurities 440
  6.2 Probing dominant defects by photoexcitation spectroscopy 442
7. Concluding remarks 447
Acknowledgments 448
References 448

Semiconductors and Semimetals, Volume 107
ISSN 0080-8784
https://doi.org/10.1016/bs.semsem.2021.04.008

Copyright © 2021 Elsevier Inc.
All rights reserved.

1. Introduction

Boron-nitride (BN) has a comparable energy band gap to AlN but is much less understood. BN has attracted a great deal of attention recently for its potential applications in deep UV (DUV) optoelectronics (Dahal et al., 2011; Jiang and Lin, 2014; Jiang et al., 2015; Kubota et al., 2007; Li et al., 2012; Majety et al., 2012a; Watanabe and Taniguchi, 2009; Watanabe et al., 2004, 2009) and solid-state neutron detection (Ahmed et al., 2017; Doan et al., 2014a, 2016a; Doty, 2004; Grenadier et al., 2019; Li et al., 2011; Maity et al., 2016, 2017a, 2018, 2019a, 2020; Uher et al., 2007). This is due to its extraordinary physical properties, such as high energy band gap ($E_g > 6$ eV) (Arnaud et al., 2006; Cao et al., 2013; Doan et al., 2016b; Huang et al., 2012; Majety et al., 2012b; Wirtz et al., 2006), large optical absorption for the above band-edge photons (Li et al., 2012; Sugino et al., 1997; Zunger et al., 1976), high electrical resistivity (Doan et al., 2014a, 2016a; Grenadier et al., 2019; Li et al., 2011; Maity et al., 2016, 2017a, 2018, 2019a, 2020; Rumyantsev et al., 2001), high chemical stability, high lateral thermal conductivity (Rumyantsev et al., 2001), and the large thermal neutron capture cross-section of the Boron isotope, Boron-10 (^{10}B) (Ahmed et al., 2017; Doan et al., 2014a, 2016a; Doty, 2004; Grenadier et al., 2019; Knoll, 1995; Li et al., 2011; Maity et al., 2016, 2017a, 2018, 2019a, 2020; Osberghaus, 1950; Uher et al., 2007). BN exists in various crystalline forms. However, the sp^2-bonded hexagonal form (h-BN) is the most stable phase when synthesized at any temperature under ambient pressure (Lynch and Drickamer, 1966; Madelung and Landolt-Bornstein, 1987; Pease, 1952; Rumyantsev et al., 2001). Because h-BN has a close lattice match to graphite and high electrical resistivity, it is recognized as the most suitable substrate/dielectric/separation layer for the construction of two dimensional (2D) heterostructures due to its ability to provide an atomically flat surface with minimal density of dangling bonds and charge traps (Alem et al., 2009; Britnell et al., 2012; Chopra et al., 1995; Dean et al., 2010, 2012; Geim and Grigorieva, 2013; Rubio et al., 1994). Like graphene, h-BN is expected to possess rich new physics due to its layered structure with the exception that it is also complementary to graphene because of its wide bandgap.

Historically, BN is considered an excellent electrical insulator and thermal conductor. More recently, lasing action and light emitting devices in the DUV region under electron-beam pump have been demonstrated (Kubota

et al., 2007; Watanabe and Taniguchi, 2009; Watanabe et al., 2004, 2009). Novel optical properties have been explored in small h-BN bulk crystals synthesized by high pressure/temperature techniques as well as by metal flux techniques at atmospheric pressure (Caldwell et al., 2019; Cao et al., 2013; Kubota et al., 2007; Watanabe and Taniguchi, 2009; Watanabe et al., 2004, 2009). These recent studies bring out the potentials of h-BN as a DUV semiconductor photonic material. So far, h-BN bulk crystals with sizes up to millimeters can be grown. Other than small size, bulk crystal growth has the added challenges in the control of growth conditions such as intentional doping and formation of device structures. As such, bulk crystal growth is most suitable for producing substrates if a relatively large size can be realized. Studies on h-BN films have been mostly performed on manually exfoliated individual layers from small h-BN bulk crystals (Alem et al., 2009; Britnell et al., 2012; Dean et al., 2010, 2012). This has been effective for the study of new physics, but prohibits the realization of wafer-scale processing, heterostructure design, and doping processes, which are prerequisites for practical device implementation. The ability to synthesize wafer-scale semiconducting h-BN epitaxial layers with high crystalline quality and electrical conductivity control is highly desirable for fundamental understanding as well as for the exploration of emerging applications of this interesting material system (Jiang and Lin, 2017).

The growth of h-BN thin films by epitaxial growth techniques such as metal organic chemical vapor deposition (MOCVD) has been successfully demonstrated by many research groups recently (Ahmed et al., 2017; Chubarov et al., 2014; Chugh et al., 2018; Dahal et al., 2011; Doan et al., 2014a, 2016a; Du et al., 2016; Grenadier et al., 2019; Jiang and Lin, 2014, 2017; Jiang et al., 2015; Kobayashi et al., 2008; Li et al., 2011, 2012, 2016; Maity et al., 2016, 2017a, 2018, 2019a, 2020; Majety et al., 2012a; Nakamura, 1986; Uddin et al., 2014a; Yang et al., 2018, 2020). Fundamental optical and electrical transport properties of h-BN epilayers are being investigated. It was shown that the unique layered structure of h-BN epilayers induces exceptionally high density of states, large exciton binding energy and high optical absorption and emission intensity (Arnaud et al., 2006; Cao et al., 2013; Doan et al., 2016b; Huang et al., 2012; Li et al., 2012; Majety et al., 2012b; Sugino et al., 1997; Wirtz et al., 2006; Zunger et al., 1976). Photocurrent excitation spectroscopy results provided a room temperature direct bandgap value for h-BN epilayers of ~6.4 eV and a free exciton binding energy (E_x) of ~0.73 eV (Doan et al., 2016b). By growing h-BN epilayers under high V/III ratios, epilayers exhibiting pure free

exciton emission at low temperatures have been obtained (Du et al., 2016). Large wafers of both natural and Boron-10 enriched h-BN epilayers (abbreviated as h-^{10}BN or ^{10}BN) epilayers of 4-in. in diameter have been successfully produced recently by MOCVD by the authors' group (Grenadier et al., 2019; Maity et al., 2016, 2017a, 2018, 2019a, 2020), as illustrated in Fig. 1. Due to its unique hexagonal (layered) structure shown in Fig. 1A and the difference in thermal expansion coefficients between h-BN and the sapphire substrate, a thick h-BN epilayer tends to automatically separate from the sapphire substrate during cooling down after growth. This forms a freestanding h-BN epilayer, as illustrated in Fig. 1B, where a photo of a freestanding h-^{10}BN wafer of 4-in. in diameter is shown (Grenadier et al., 2019; Maity et al., 2016, 2017a, 2018, 2019a, 2020). As seen in Fig. 1D and E, these h-^{10}BN freestanding epilayers can be diced into desired sizes and shapes, can be re-grouped to form large arrays and are flexible (Grenadier et al., 2019; Maity et al., 2016, 2017a, 2018, 2019a, 2020), thereby offering the potential to attach to rigid, flat or curved surfaces. As of today, freestanding h-^{10}BN epilayers with a thickness up to 200 μm have been produced by MOCVD by the authors' group (Fig. 1F). Furthermore, the growth of layer-structured (BN)-rich h-BGaN and h-(BN)C alloys, heterostructures, and quantum wells (QWs) and their optical properties have also been explored for the feasibility of bandgap engineering in h-BN (Uddin et al., 2014a,b; Wang et al., 2019a,b).

As with all semiconductor materials, the ability to control conductivity is highly desirable to realize technologically significant devices based on h-BN. However, experimental studies on the transport properties of intentionally doped *h*-BN thin films with the aim of obtaining conductivity control have been limited (Dahal et al., 2011; He et al., 2009, 2014; Jiang and Lin, 2014; Lu et al., 1996; Majety et al., 2012a, 2013a; Nose et al., 2006; Sugino et al., 1997; Uddin et al., 2017). Earlier studies suggested the existence of a negative electron affinity at the surface of BN films and that BN has properties like diamond (Powers et al., 1995; Sugino et al., 1997). Consequently, it was expected that p-type h-BN may be more readily obtained than n-type as in the case of diamond. As such, one of the initial motivations of developing MOCVD growth processes for h-BN epilayers was to exploit a novel DUV emitter concept to potentially overcome the intrinsic problem of low p-type conductivity (or low free hole concentration) in Al-rich AlGaN (Dahal et al., 2011; Jiang and Lin, 2014; Jiang et al., 2015; Majety et al., 2012a). Fig. 2 illustrates the basic proposed DUV emitter layer structure based on h-BN and AlN heterojunction and doping engineering

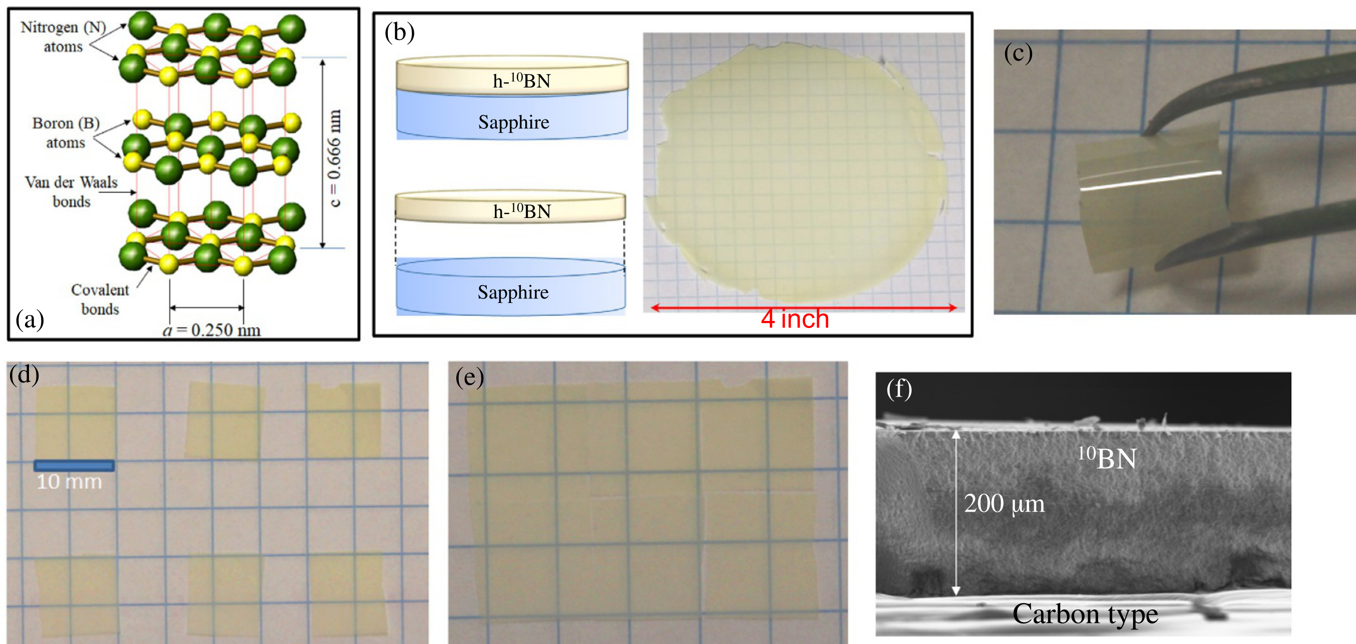

Fig. 1 (A) Schematic illustration of the crystal structure of h-BN. (B) Illustration of the formation and photograph of a freestanding ^{10}B-enriched h-BN (h-^{10}BN) wafer of 4-in. in diameter. (C) Photograph of a representative freestanding h-^{10}BN layer with a thickness of 50 µm showing its flexibility. (D) Small pieces of diced h-^{10}BN samples. (E) Small pieces of diced h-^{10}BN samples reassembled into a single piece. (F) SEM image cross-sectional view of a h-^{10}BN epilayer of 200 µm in thickness, all produced by the authors.

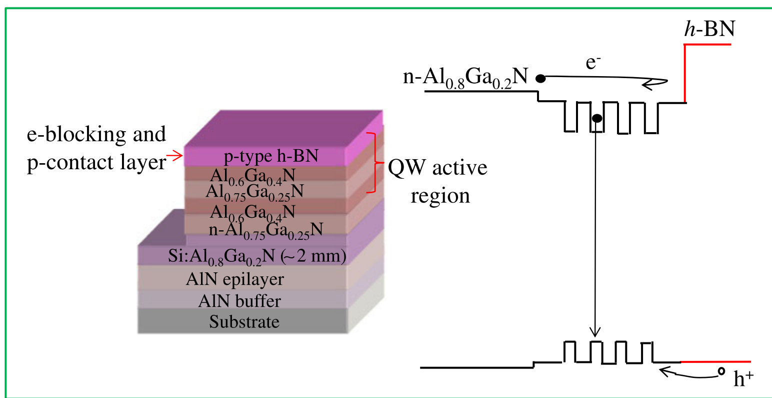

Fig. 2 Schematic of a deep UV emitter layer structure using p-type h-BN. The wide bandgap p-type h-BN serves as a natural electron-blocking, hole injection, and p-type contact layer. The corresponding energy band diagram is also illustrated. *Reproduced from Jiang, H.X., Majety, S., Dahal, R., Li, J., Lin, J.Y., 2021. Structures and Devices Based on Boron Nitride and Boron Nitride-III-Nitride Heterostructures. US patent #9,093,581.*

(Jiang and Lin, 2014; Jiang et al., 2015). By implementing a h-BN p-type layer strategy in nitride DUV emitters, it was anticipated that the p-type conductivities of the electron blocking, hole injection, and the p-type contact layers in the DUV emitter structure will be increased. Furthermore, theoretical and experimental studies have revealed that the band alignment in h-BN and wurtzite (w)-AlN (and Al-rich AlGaN) heterojunctions is type II with a small valence band offset (Hao et al., 2019; Jiang and Lin, 2014; Jiang et al., 2015; Majety et al., 2013b), meaning that the band edges of h-BN moved upwards with respect to those of w-AlN, however without introducing any significant energy barrier for hole injection as illustrated in the band diagram of Fig. 2 (Jiang and Lin, 2014; Jiang et al., 2015). It was hoped that these properties together would improve the free hole injection, electron blocking and quantum efficiency, reduce the contact resistance, operating voltage and heat generation, and increase the device efficiency, operating lifetime and UV transparency. On the other hand, n-type conductivity control via in-situ doping with Si, C and Zn have also been attempted with limited success. As of today, high performance DUV devices based on h-BN p-n junction epitaxial layers have not yet been demonstrated.

The most successful devices demonstrated from h-BN epilayers are thermal neutron detectors based on Boron-10 enriched h-BN epilayers

(Doan et al., 2014a, 2016a; Grenadier et al., 2019; Li et al., 2011; Maity et al., 2016, 2017a, 2018, 2019a, 2020). Neutron detectors have applications in geothermal and oil well logging where they are used to provide information for porosity evaluation, gas detection, shale evaluation, and borehole corrections (Neal et al., 2011). When a fast neutron emitted from a neutron generator strikes a hydrogen nucleus of equal mass, which is present in pore water/oil, it thermalizes. To the first order, the thermal neutron count is inversely proportional to the hydrogen content (or the porosity) of the surrounding geology. National security is another major end user of neutron detectors, which are employed to identify the signatures of special nuclear materials and sense any illicit movement of fissile materials at ports of entry (Noonan, 2014). Modern neutron logging tools commonly count thermal (0.025 eV) and epithermal (0.025–0.4 eV) neutrons by employing pressurized ${}^{3}_{2}He$ (He-3) gas tube detectors. However, being a gas, He-3 detectors are inherently bulky. Other shortcomings of He-3 detectors are the need of high pressurization and slow response speed (∼ms). These attributes prohibit flexibilities in detector design and form factors and increase exploration/logging time and maintenance costs. Additionally, He-3 gas detectors are most appropriate for operation below 175 °C. For well logging, the trend is moving into deep and slim wells where temperatures easily exceed 250 °C. For geothermal logging, the environmental conditions are even more extreme where temperatures can be as high as 500 °C. Therefore, solid-state neutron detectors with enhanced capabilities of operating in extreme environments of high temperatures/mechanical vibration/shock are highly desirable. Because it is composed of low atomic number elements, B(5) and N(7), h-BN's interaction with gamma photons is extremely low, which gives rise to an excellent gamma to neutron discrimination ratio (below 10^{-6}) for BN neutron detectors (Doan et al., 2014a, 2016a; Maity et al., 2016, 2020).

Thermal neutron detectors of photoconductive-type fabricated from thick freestanding h-^{10}BN epilayers have demonstrated a detection area of 1 cm^2 with a record high thermal neutron detection efficiency among solid-state neutron detectors at 59%, as of this writing (Maity et al., 2020). These detectors do not require the ability of conductivity control for BN. Once matured, the adoption of BN solid-state detector technology is expected to reduce the downtime due to logging equipment failures, which are very expensive as "the cost of running operations on an offshore drilling rig is very high: drilling a well might cost $1–2 million per day of operations," according to a National Research Council report (National Research Council, 2008). Thousands of new wells were drilled in the last

10 years. Even a fraction reduction in equipment failures could contribute to a cumulative of hundreds of millions of dollars in cost savings. Moreover, BN detector technology will also create opportunities for the exploration of new energy materials in previously inaccessible areas. As such, the impact on new energy resource discovery is expected to be huge. Novel neutron detectors will also aid in the production of safe nuclear energy. However, photoconductive-type neutron detectors exhibit unique requirements in terms of material quality and electrical transport properties.

2. Prospects of n- and p-type doping of h-BN

2.1 Mg doping

Epitaxial layers of h-BN were synthesized by MOCVD using triethylboron (TEB) and ammonia (NH_3) as B and N precursors, respectively (Dahal et al., 2011; Jiang et al., 2015; Jiang and Lin, 2014; Li et al., 2012; Majety et al., 2012a). To account for the lattice mismatch between h-BN and sapphire, a low temperature h-BN buffer layer was first deposited on sapphire substrate at 800 °C. A set of samples were grown with buffer thicknesses varying from 140 to 20 nm. Experimental results indicated that with decreasing thickness of the buffer layer, the X-ray diffraction (XRD) intensity of the h-BN (0002) reflection peak increases and the full width at half maxima (FWHM) of the h-BN (0002) reflection peak decreases. Thus, a thinner buffer seemed to yield epilayers with better quality (Dahal et al., 2011; Jiang and Lin, 2014; Majety et al., 2012a). For the growth of Mg doped h-BN epilayers (h-BN:Mg), biscyclopentadienyl-magnesium was transported into the reactor during h-BN epilayer growth. Mg doping concentration in the epilayers was about $1 \times 10^{19}\,cm^{-3}$, as verified by secondary ion mass spectrometry (SIMS) measurement (Dahal et al., 2011; Jiang and Lin, 2014; Majety et al., 2012a). It was found that like Mg doped AlGaN alloys, post growth thermal annealing was helpful to activate the Mg acceptors in h-BN. We found that the "optimal" p-type material annealing conditions include an annealing temperature of about 1150 °C and annealing time of about 45 min. Obviously, these conditions will need to be continuously refined as the growth processes of h-BN epilayers continue to evolve.

Previously reported results showed strong evidence that the acceptor activation energy in h-BN is smaller than that in AlN. The measured acceptor energy levels were 0.3 eV and 0.15 eV for Mg and Zn doped BN films of mixed phases prepared by CVD, sputtering, and ion implantation (He et al., 2009; Lu et al., 1996; Nose et al., 2006). Based on the temperature

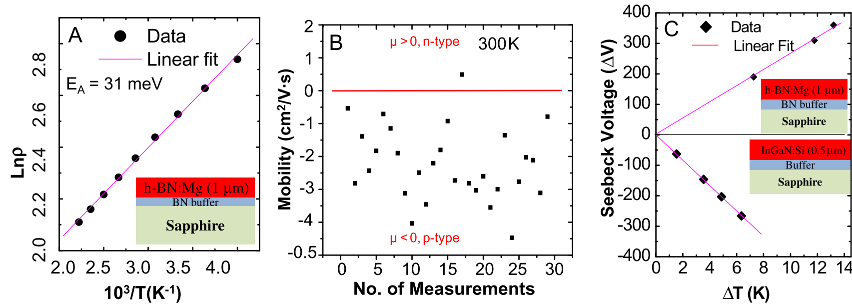

Fig. 3 (A) p-type resistivity as a function of temperature of an h-BN:Mg epilayer as a semi-log plot, yielding an activation energy of about 31 meV. (B) Confirmation of p-type conduction in h-BN:Mg at 300 K is demonstrated by mobility (μ) measurements. In the setup, $\mu > 0$ indicates electron conduction and $\mu < 0$ indicates hole conduction. The measured data provide an average hole mobility of $\sim 2\,cm^2/V \cdot s$. (C) Seebeck coefficient measurements from a h-BN:Mg sample and n-type $In_{0.3}Ga_{0.7}N$:Si sample (with $n = 3 \times 10^{19}\,cm^{-3}$ and $\mu = 90\,cm^2/V \cdot s$). These measurements confirm unambiguously that h-BN:Mg epilayers are p-type. *Reproduced from Dahal, R., Li, J., Majety, S., Pantha, B.N., Cao, X.K., Lin, J.Y., Jiang, H.X., 2011. Epitaxially grown semiconducting hexagonal boron nitride as a deep ultraviolet photonic material. Appl. Phys. Lett. 98, 211110; Copyright (2011) AIP Publishing.*

dependent resistivity measurement shown in Fig. 3A, the estimated activation energy of Mg acceptors (E_A) in h-BN:Mg epilayers grown by MOCVD was significantly smaller than that of Mg in AlN epilayers (Dahal et al., 2011). The hole mobility of a h-BN:Mg epilayer was evaluated multiple times using Hall-effect measurements and the results are summarized in Fig. 3B. Although the mobility data shown in Fig. 3B is accompanied with a large fluctuation due to the low hole mobility of this set of samples, the results confirmed p-type conduction with a free hole concentration of p $\sim 10^{18}\,cm^{-3}$ and an average mobility $\mu \sim 2\,cm^2/V \cdot s$. Moreover, Seebeck effect measurements (hot probe) were also performed to further confirm the conductivity type of h-BN:Mg epilayers (Dahal et al., 2011). As shown in Fig. 3C, the Seebeck coefficient for a Si doped and strongly n-type $In_{0.3}Ga_{0.7}N$ epilayer (with $n = 3 \times 10^{19}\,cm^{-3}$ and $\mu = 90\,cm^2/V \cdot s$) was $S = \Delta V/\Delta T + S_{Alumel} = -42.2 - 18.5 = -60.7\,\mu V/K$, whereas that for h-BN:Mg was $S = \Delta V/\Delta T + S_{Alumel} = 28.0 - 18.5 = 9.5\,\mu V/K$. The sign reversal in S over n-type $In_{0.3}Ga_{0.7}N$:Si sample confirms unambiguously that these h-BN:Mg epilayers are p-type (Dahal et al., 2011; Jiang and Lin, 2014).

The feasibility of depositing h-BN epilayers on AlN templates has been investigated to lay the foundation for the DUV structure shown in Fig. 2 (Jiang and Lin, 2014; Jiang et al., 2015; Majety et al., 2012a). There is a large

lattice mismatch between h-BN and AlN (in plane lattice constants of 2.5 Å and 3.1 Å, respectively). Although the lattice mismatch is about 19.54% when h-BN epilayer is grown on a c-plane AlN epilayer, we noticed that the 4 *a*-lattice constant of AlN (4 $a_{AlN} = 4 \times 0.3112\,nm = 1.245\,nm$) is almost the same as the 5 *a*-lattice constant of h-BN (5 $a_{BN} = 5 \times 0.2504\,nm = 1.252\,nm$) (Jiang and Lin, 2014; Jiang et al., 2015; Majety et al., 2012a). This means that every 5 h-BN atoms will align with 4 AlN atoms along the *a*-direction. This 5/4 coincidence in the h-BN/w-AlN heterojunction interface reduces the effective lattice mismatch from 19.54% to about 0.58%, making the epitaxial growth of h-BN and AlN heterostructures possible (Jiang and Lin, 2014; Jiang et al., 2015; Majety et al., 2012a).

The highly insulating nature of AlN allows the electrical properties of Mg doped h-BN to be characterized. P-contacts consisting of 30-nm-thick Ni were deposited using e-beam evaporation. The metal contacts were subjected to thermal annealing to investigate the change in contact resistance with different annealing conditions. This was done by measuring the I-V characteristics. As shown in Fig. 4A, it was observed that thermal annealing the Ni contacts at 1020 °C for 1 min significantly reduced the contact

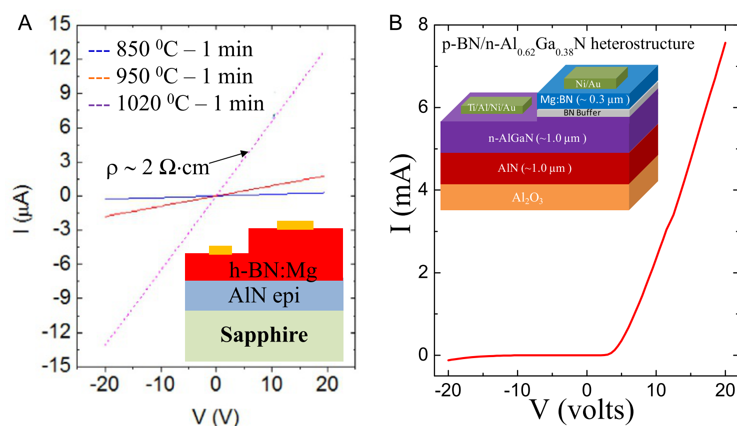

Fig. 4 (A) The I-V characteristics of p-type h-BN:Mg epilayers deposited on highly insulating AlN with Ni contacts thermally annealed at different temperatures. (B) I-V characteristics and schematic illustration of a p-BN:Mg/n-$Al_{0.62}Ga_{0.38}N$:Si/AlN p-n structure in which the buffer layer was doped with Mg and p-contacts were thermal annealed at 1020 °C for 1 min, exhibiting a diode behavior. *Reproduced from Majety, S., Li, J., Cao, X.K., Dahal, R., Pantha, B.N., Lin, J.Y., Jiang, H.X., 2012. Epitaxial growth and demonstration of hexagonal BN/AlGaN p-n junctions for deep ultraviolet photonics. Appl. Phys. Lett. 100, 061121; Copyright (2012) AIP Publishing.*

resistance. The lowest p-type resistivity observed for Mg doped h-BN samples grown on AlN templates was around ~2 Ω·cm, which is several orders of magnitude lower than those of Mg doped Al-rich AlGaN alloys and AlN epilayers. For instance, the typical room temperature resistivity is about 10^7 Ω·cm for Mg doped AlN (Nakarmi et al., 2006) and is (4–13) × 10^4 Ω·cm for Mg doped $Al_{0.7}Ga_{0.3}N$ alloy epilayers (Nakarmi et al., 2005). Although, practical DUV emitters which incorporate p-type h-BN epilayers have not yet been demonstrated, a p-BN/n-AlGaN heterostructure as shown in Fig. 4B has been produced (Majety et al., 2012a) and explored for DUV device applications, which can be further improved to tackle the p-type conductivity issue in DUV emitters based on high Al-content AlGaN alloys.

More recently, very favorable results have been demonstrated for AlGaN nanowire based DUV LED structures by utilizing h-BN as a p-type current injection layer (Laleyan et al., 2017). However, it is interesting to note that the nanowire h-BN/n-AlN DUV LED structures are Mg-dopant free, whereas the p-type conduction was attributed to the possible formation of native defects such as boron vacancies which act as acceptors (Laleyan et al., 2017). The observation of free holes in Mg-dopant free h-BN nanowires seems to be consistent with high temperature Hall-effect measurement results performed on an unintentionally doped thin h-BN epilayer of about 1.7 μm grown at around 1300 °C shown in Fig. 5, which demonstrated that this epilayer is a semiconductor exhibiting a weak p-type conduction at high temperatures (>700 °K) with a measurable free hole concentration of about 3×10^{14} cm^{-3} and in-plane hole mobility of about 13 cm^2/V·s, providing an in-plane p-type resistivity of ~1.6×10^3 Ω·cm at 790 °K (Doan et al., 2014b). This seems to imply that the Fermi level in undoped *h*-BN lies below the middle of the energy gap and undoped h-BN materials tend to be slightly p-type. In this sense, h-BN is more like diamond than other III-nitride semiconductors. The temperature dependent electrical resistivity of this undoped epilayer shown in Fig. 5C yielded an acceptor energy level of about 0.68 eV above the valence band with a possible origin attributed to boron vacancies V_B, or V_B related defects (Doan et al., 2014b).

Moreover, the carrier mobility lifetime, μτ, product measurements conducted on an unintentionally doped h-^{10}BN epilayer revealed a larger μτ product for holes than for electrons, again implying that holes (electrons) behave like majority (minority) carriers in unintentionally doped h-BN (Maity et al., 2016). Furthermore, a recent high-resolution angle-resolved photoemission spectroscopy measurement performed on h-BN films deposited on graphene has revealed that the valence-band maxima in h-BN are

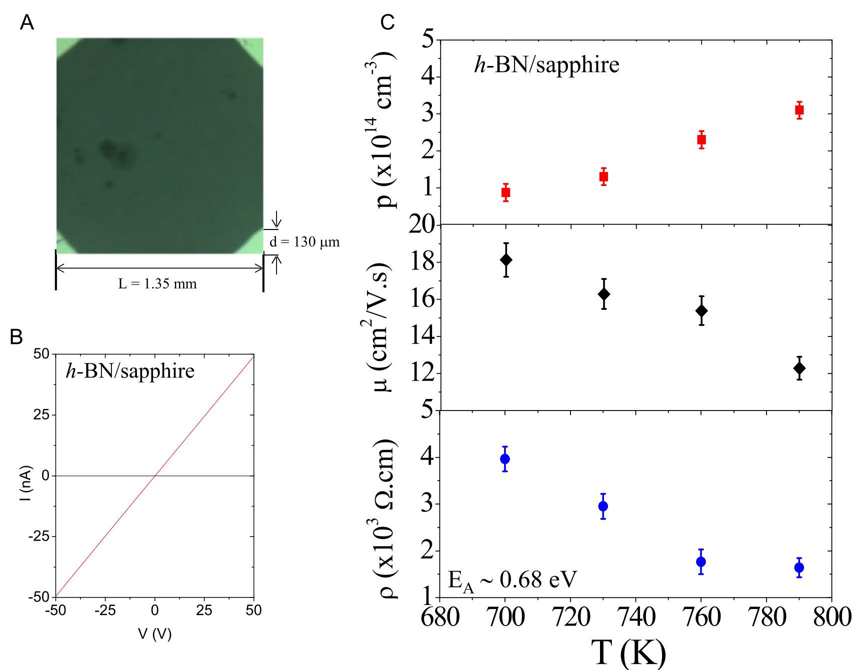

Fig. 5 (A) Optical image of an unintentionally doped 1.7 μm thick h-BN epilayer grown at 1300 °C with ohmic contacts [Ni/Au (20 nm/30 nm)] on the four corners for Van der Pauw–Hall measurements. (B) Room temperature I-V characteristics of the unintentionally doped h-BN epilayer. (C) The temperature dependence of hole concentration (p), hole mobility (μ), and p-type resistivity (ρ) of an unintentionally doped h-BN epilayer measured from 700 to 790 K. *Reproduced from Doan, T.C., Li, J., Lin, J.Y., Jiang, H.X., 2014. Charge carrier transport properties in layer structured hexagonal boron nitride. AIP Adv. 4, 107126; Copyright (2014) AIP Publishing.*

located around the *K* points, 2.5 eV below the Fermi level, and hence inferred the residual *p*-type character of typical h-BN (Henck et al., 2017).

2.2 Si doping

For n-type doping, it seems that Si would be a natural choice as an n-type dopant, as it has been established for GaN and AlN. The incorporation of Si and S into cubic-BN (c-BN) films or films with mixed c-BN/h-BN phases by in-situ doping techniques has also been examined and the microstructures, mechanical properties as well as the field emission characteristics have been studied for these films (Sugino et al., 1997; Ying et al., 2011). Recently, the suitability of Si as an n-type dopant in h-BN has been investigated (He et al., 2014; Majety et al., 2013a). It was found that for all Si doped h-BN epilayers (h-BN:Si) grown by MOCVD annealed at different

conditions, the n-type resistivity was too high to prevent Hall effect measurements at room temperature (Majety et al., 2013a). Hall effect measurements were carried out at 850 K for an "optimized" sample and yielded an average resistivity $\rho \sim 12\,\Omega\cdot cm$ with a free electron concentration (n) of $\sim 1 \times 10^{16}\,cm^{-3}$ and mobility (μ) of $\sim 48\ (\pm 24)\ cm^2/V\cdot s$. The mobility data shown in Fig. 6A is accompanied by a large fluctuation, however, is unambiguously confirming n-type conductivity of h-BN:Si. The temperature dependent resistivity shown in Fig. 6B and C yielded an energy level of Si in h-BN of $E_D \sim 1.2\,eV$, which is quite deep. The measured Si energy level of 1.2 eV agrees well with that of a calculation, which implied an energy level of Si of about 1.1 eV in h-BN (Oba et al., 2010). The results shown in Fig. 6 seem to suggest that Si is not a suitable n-type dopant for h-BN for room temperature applications. However, n-type conductivity in h-BN polycrystalline thin films synthesized by magnetron sputtering on quartz and Si substrates has been obtained via Si ion implantation (He et al., 2014) and the temperature-dependent resistivity measurements revealed that Si in polycrystalline h-BN is a shallow level with an activation energy of 15 meV measured in 50–300 K and 60 meV in 300–800 K (He et al., 2014). A density functional theory (DFT) calculation based on an h-BN monolayer model containing 1000 atoms by the same authors suggested that the substitutional Si induces a state at $\sim 177\,meV$ (He et al., 2014). Following the footsteps of III-nitrides, it is well known that only insulating Al-rich $Al_xGa_{1-x}N$ alloys ($x > 0.5$) can be obtained prior to 2002 (Gorczyca et al., 2002; Lyons et al., 2014; Mattila and Nieminen, 1997; Nakarmi et al., 2004; Nam et al., 2002, 2005; Nepal et al., 2006; Stampfl and Van de Walle, 1998; Zhu et al., 2004). In order to obtain highly conductive n-$Al_xGa_{1-x}N$ with high Al-contents, it was critical to minimize the density of native defects (mainly group III vacancies) and carbon impurities occupying the nitrogen sites (C_N), which act as the free electron compensating centers (or electron traps) (Gorczyca et al., 2002; Lyons et al., 2014; Mattila and Nieminen, 1997; Nakarmi et al., 2004; Nam et al., 2002, 2005; Nepal et al., 2006; Stampfl and Van de Walle, 1998; Zhu et al., 2004). Therefore, it may be still worthwhile to further investigate Si doping in h-BN epilayers under different doping and growth conditions.

2.3 Carbon doping

A recent theoretical study has indicated that substitutional carbon, carbon occupying boron site (C_B), is a donor in monolayer *h*-BN (Fujimoto and Saito, 2016). The calculated activation energy (E_D) of C_B donors in

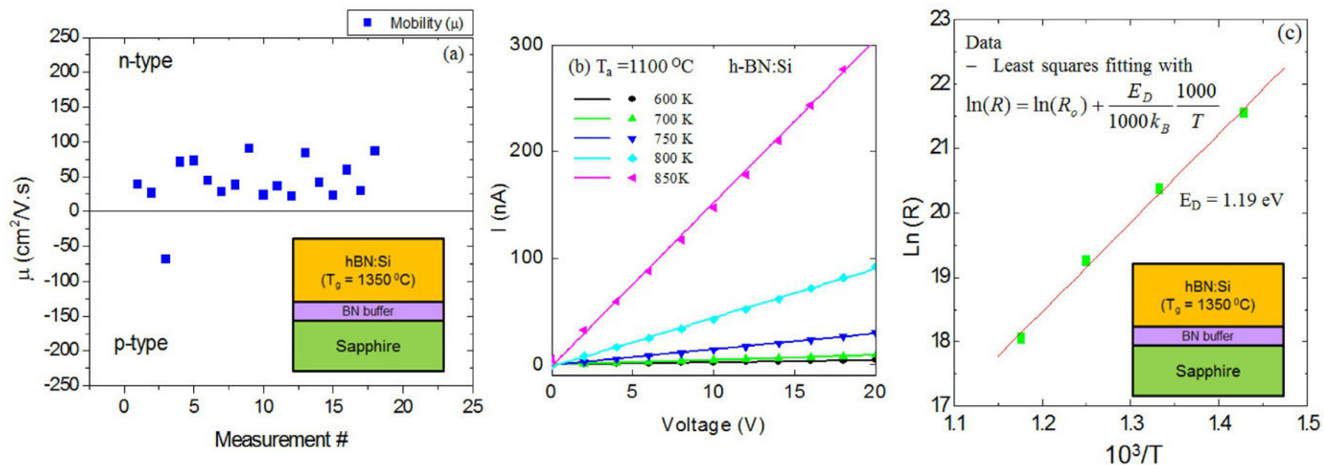

Fig. 6 (A) Mobility data obtained by Hall effect measurements carried out at 850 K for an h-BN:Si sample, thermally annealed at a temperature of $T_a = 1100$ °C after growth. In the experimental setup, $\mu > 0$ indicates electron conduction and $\mu < 0$ indicates hole conduction. (B) I-V characteristics of the same h-BN:Si sample measured at different temperatures. (C) n-type resistivity as a function of temperature of the same h-BN:Si sample measured at $T > 700$ K, yielding an activation energy for Si donors of about 1.19 eV. *Reproduced from Majety, S., Doan, T.C., Li, J., Lin, J.Y., Jiang, H.X., 2013. Electrical transport properties of Si-doped hexagonal boron nitride epilayers. AIP Adv. 3, 122116; Copyright (2013) AIP Publishing.*

monolayer *h*-BN is about 0.94 eV (Fujimoto and Saito, 2016). In general, the ionization energy of donors (and acceptors) is expected to increase as the dimensionality of *h*-BN scales from bulk to monolayer due to the enhanced in-plane overlap among carriers and impurities as well as the reduced screening. In theory, E_D will increase by a factor of 4 as the dimensionality of a semiconductor scales from bulk to 2D, which implies that E_D could be as low as 0.24 eV in bulk *h*-BN. This argument makes carbon a possible viable candidate for n-type doping in *h*-BN (Uddin et al., 2017).

Carbon doped (*h*-BN:C) and undoped *h*-BN epilayers of 30 nm in thickness were grown by MOCVD for comparison studies (Uddin et al., 2017). Photodetectors based on a metal-semiconductor-metal (MSM) architecture with micro-strip interdigital fingers, as shown in Fig. 7A, were fabricated from *h*-BN and *h*-BN:C epilayers for photocurrent excitation spectroscopy measurements (Uddin et al., 2017). The MSM detector has a device size of 0.5 mm × 0.5 mm with metal strips of 6 μm in width and 9 μm in spacing. The basic layer structures of *h*-BN:C and *h*-BN epilayers are shown in the insets of Fig. 7B. Fig. 7B shows the room temperature photocurrent excitation spectra of *h*-BN:C and *h*-BN epilayers. The results clearly show that carbon doping introduces additional spectroscopic features in the spectrum of *h*-BN:C compared to that of undoped *h*-BN. Fig. 7C is a replot of the photocurrent excitation spectrum of *h*-BN:C sample shown in Fig. 7B with the energy positions of the dominant transitions marked for clarity. Transition peaks observed at about 4.2, 6.0, and 6.45 eV are clearly resolved in the spectrum of the *h*-BN:C sample, while the spectrum of the undoped *h*-BN sample shown in the bottom panel of Fig. 7B exhibits primarily one transition peak at about 6.45 eV. The 6.45 eV transition peak can be assigned to the direct band-to-band excitation in *h*-BN epilayers (Doan et al., 2016b). The transition lines at about 4.2 eV and 6.0 eV are absent in undoped *h*-BN and are only associated with carbon doping.

Based on photoluminescence (PL) spectroscopy study results (Du et al., 2015), the peak at 4.2 eV can be attributed to the direct excitation of electrons from ionized acceptors to the conduction band, whereas the involved acceptors are believed to be carbon impurities occupying nitrogen site (C_N) with an energy level of about 2.3 eV above the valence band edge (Du et al., 2015). The observation of this transition peak near 4.2 eV implies that a concomitant effect of substitutional carbon doping is self-compensation. Although most incorporated carbon atoms tend to form C-C pairs in *h*-BN due to the relatively large C-C bond energy of about 3.71 eV (Bahandary and Sanyal, 2012), the presence of a fraction of isolated neutral

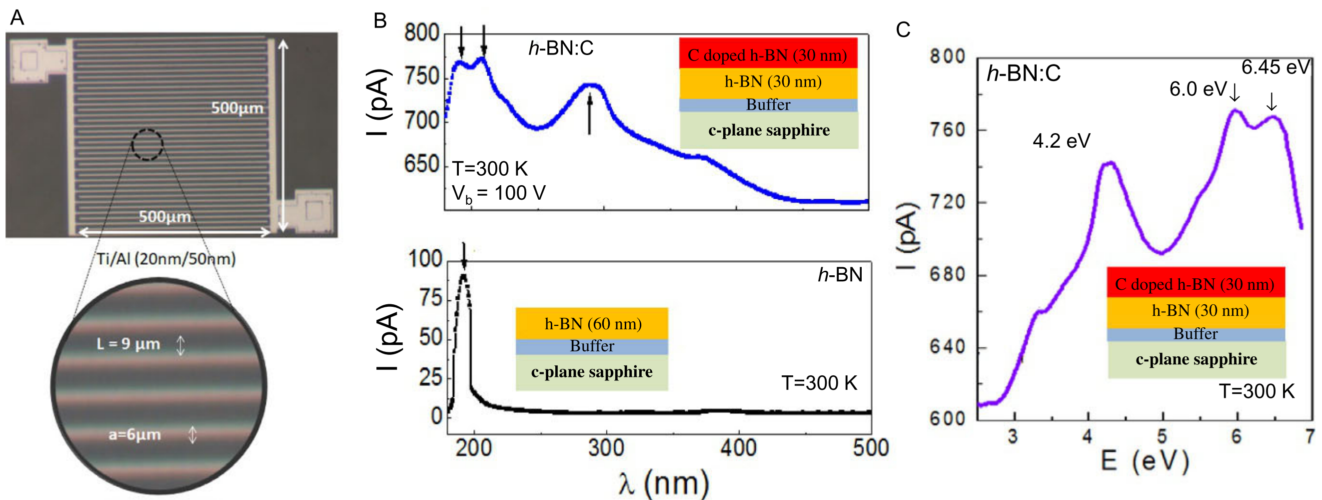

Fig. 7 (A) Microscope image of a photodetector based on the metal-semiconductor-metal (MSM) architecture with interdigital fingers fabricated from a carbon doped *h*-BN epilayer (h-BN:C). (B) Room temperature photocurrent excitation spectra of a h-BN:C and undoped h-BN epilayer. The insets are the corresponding schematic layer structures of the h-BN:C and un-doped h-BN epilayers. (C) Replot of the photocurrent excitation spectrum of an h-BN:C epilayer with peak positions marked for clarity. *Reproduced from Uddin, M.R., Li, J., Lin, J.Y, Jiang, H.X., 2017. Probing carbon impurities in hexagonal boron nitride epilayers. Appl. Phys. Lett. 110, 182107; Copyright (2017) AIP Publishing.*

donors (D^0) of carbon impurities occupying boron sites (C_B) is expected. However, self-compensation induces a fraction of ionized C_N acceptors (A^-) as well as an equal number of ionized donors (D^+). This observation is also consistent with the fact that C is a group IV element and can substitute either B acting as a donor or N acting as an acceptor (Uddin et al., 2017). The observed transition peak at about 6.0 eV in h-BN:C was attributed to the direct excitation of electrons from the valence band to ionized C_B donors (D^+). In such a framework, the energy difference between the band-to-band transition at 6.45 and the 6.0 eV transition provides an ionization energy of C_B donors in *h*-BN epilayers, which is about $E_D \approx 0.45$ eV. This value is about a factor of 2 smaller than the calculated value of 0.94 eV in monolayer *h*-BN (Fujimoto and Saito, 2016), but larger than the expected theoretical limit of $\sim \frac{1}{4}(0.94) \sim 0.24$ eV in bulk *h*-BN. This is reasonable since other factors such the quasi-2D nature of *h*-BN epilayers, strain and central-cell correction would also modify the value of E_D in *h*-BN epilayers. The energy level of C_B donors can also be estimated via temperature dependent electrical resistivity. Fig. 8 is a plot the temperature dependence of resistivity (ρ), measured from 600 to 850 °K, in a linear plot (a) and in an Arrhenius plot (b). The temperature dependent resistivity was fitted by the equation, $\rho(T) = \rho_0 \exp(E_D/KT)$, where E_D denotes the energy level of C_B donors in *h*-BN epilayers. The fitted value of E_D is about 0.45 eV, corroborating well with the E_D value of about 0.45 eV determined from the photocurrent excitation spectrum shown in Fig. 7. Since the C_N deep level acceptor concentration is directly related to the presence nitrogen vacancies, it was speculated that growing *h*-BN:C in a nitrogen-rich growth environment could help to reduce the self-compensation effect. However, other than self-compensation, the results shown in Figs. 7 and 8 suggest that the carbon donor is still too deep to be a viable candidate as an n-type dopant in *h*-BN epilayers (Uddin et al., 2017).

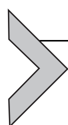

3. Criteria of h-BN as thermal neutron detector materials

Photoconductive-type neutron detectors based on h-^{10}BN epilayers have demonstrated a detection area of 1 cm^2 with an unprecedented high thermal neutron detection efficiency of 59%. This represents a record among solid-state neutron detectors, as of this writing (Maity et al., 2020). If further developed and successfully adopted to replace He-3 gas detectors used in various application areas such as in neutron logging tools, h-BN detectors are expected to provide significant performance enhancements,

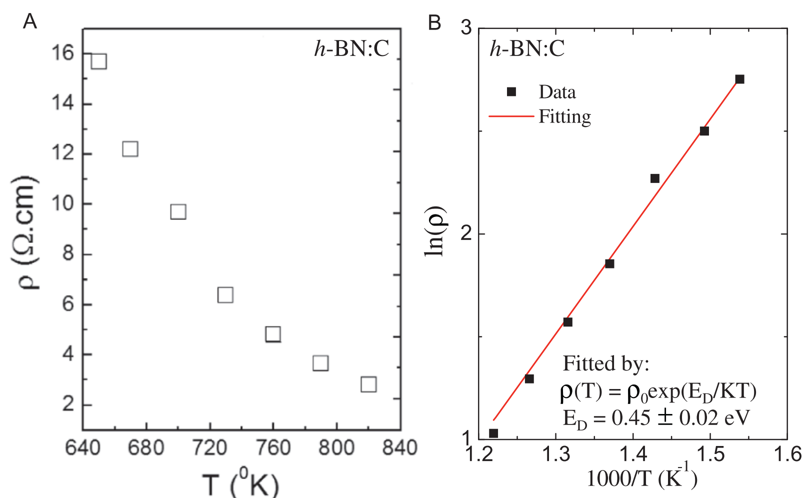

Fig. 8 The temperature dependence of the electrical resistivity, ρ, of an *h*-BN:C epilayer. *Reproduced from Uddin, M.R., Li, J., Lin, J.Y., Jiang, H.X., 2017. Probing carbon impurities in hexagonal boron nitride epilayers. Appl. Phys. Lett. 110, 182107 (2017); Copyright (2017) AIP Publishing.*

as summarized in Table 1. These include increased detection efficiency, operating temperature and ruggedness, reduced size and weight, no pressurization, lower operating voltage and power consumption as well as larger/faster signals in extreme environments which consequently decrease the required exploration/logging time as well as the costs of operation/maintenance and potentially enables the use of logging tools in harsh environments where ^{3}He gas detectors are not suitable. However, in order to obtain high detection efficiencies (η), h-^{10}BN layers with a thickness greater than 50 μm are necessary in order to provide sufficient thermal neutron absorption or high intrinsic detection efficiency. Furthermore, neutron detection efficiency not only depends on the epilayer thickness, but also depends on charge collection efficiency (η_c), which is determined by the overall material quality. Therefore, high performance BN neutron detectors require certain criteria in terms of key material parameters including thickness, electrical resistivity, and carrier mobility and lifetime products.

3.1 Thickness requirement

The element B exists as two main stable isotopes, ^{10}B and ^{11}B in a natural abundance of approximately 20% and 80%, respectively (Knoll, 1995; Osberghaus, 1950). However, only the isotope ^{10}B can interact strongly

Table 1 Characteristics comparison between He-3 gas tube detectors and ^{10}BN detectors for geothermal and well logging.

	He-3 gas detector	**^{10}BN semiconductor detector**
Nuclear reaction	$^{3}He + ^{1}n = ^{1}H$ (573 keV) + ^{3}H (191 keV)	$^{10}_{5}B + ^{1}_{0}n = ^{7}_{3}Li^{*}$ (0.84 MeV) + $^{4}_{2}\alpha^{*}$ (1.47 MeV), 94% $^{10}_{5}B + ^{1}_{0}n = ^{7}_{3}Li$ (1.015 MeV) + $^{4}_{2}\alpha$ (1.777 MeV), 6% Li, $\alpha \rightarrow N\ (e^{-}) + N\ (h^{+})$, $N \sim 10^{5}$
Intrinsic efficiency for (0.025 eV) thermal neutrons	77% ($\phi = 1''$ @ 4 atm)	88% (100 μm thick)
Intrinsic efficiency for (0.4 eV) epithermal neutrons	20% ($\phi = 1''$ @ 4 atm)	63% (200 μm thick)
Method for increasing sensitivity	Increase gas tube diameter, length, pressure	Increase the thickness and total detection area of the h-^{10}BN detector chip
Response speed	~1 ms	~μs
Operating voltage (V)	>1000	<500
Typical operating temperature, °C	−50 to +150	−200 to +500
Gamma rejection ratio	$\sim 1 \times 10^{-4}$	$\sim 1 \times 10^{-6}$
Energy resolution	6%	3%
Active volume ratio for equivalent sensitivity	300–500 (depending on the gas tube diameter and pressure)	1
Cost for equivalent sensitivity	\$2400 ($\phi = 1''$; L = 25 cm @ 4 atm)	~\$240 ($2 \times 2''$ wafers, 100 μm thick)

Notes: Both He-3 and h-BN detectors exhibit very little response to fast neutrons (neutrons with E > 0.1 MeV).
Scintillator detectors are sensitive to both thermal neutrons and gamma photons and require additional methods to discriminate thermal neutrons from gamma photons.

with neutrons. Fig. 9A shows that ^{10}B has a large capture cross section (σ) of 3840 b ($= 3.84 \times 10^{-21}$ cm^2) for thermal neutrons (neutrons with an average energy = 25 meV), which is only slightly smaller than a value of σ ~5330 b for He-3 (Knoll, 1995). However, as a semiconductor, the density of atoms which can interact with thermal neutrons in 100% ^{10}B-enriched

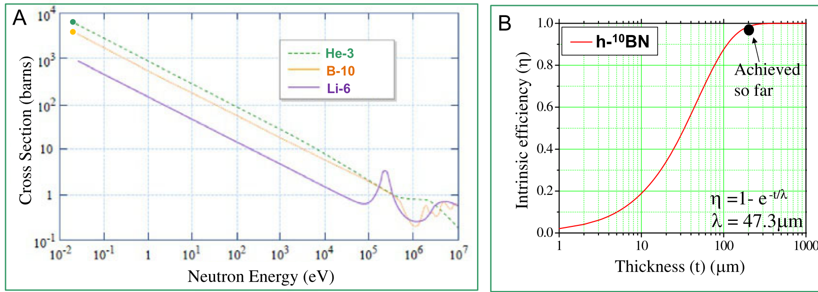

Fig. 9 (A) Neutron capture cross sections as functions of the kinetic energy of neutrons for He-3, B-10, and Li-6. The green and orange dots indicate, respectively, the cross sections of He-3 and B-10 for thermal neutrons (neutrons with an average energy of 0.025 eV). (B) Plot of Eq. (1)—The theoretical thermal neutron detection efficiency of 100% ^{10}B-enriched h-BN with respect to the h-BN epilayer thickness. *Panel (A): Credit: MIT OpenCourseWare—https://ocw.mit.edu/courses/nuclear-engineering/22-106-neutron-interactions-and-applications-spring-2010/lecture-notes/MIT22_106S10_lec07.pdf—Slide 27. Panel (B): Reproduced from Maity, A., Doan, T.C., Li, J., Lin, J.Y., Jiang, H.X., 2016. Realization of highly efficient hexagonal boron nitride neutron detectors. Appl. Phys. Lett. 109, 072101; Copyright (2016) AIP Publishing.*

BN is $N(^{10}B) = 5.5 \times 10^{22}/cm^3$ and is about 550 times higher than that in a typical He-3 gas tube pressurized at 4 atm. This provides an absorption coefficient of $\alpha = N\sigma = 5.5 \times 10^{22} \times 3.84 \times 10^{-21} = 211.2\ cm^{-1}$ and an absorption length of $\lambda = \alpha^{-1} = 47.3\ \mu m$ (Doan et al., 2014a; Maity et al., 2016).

The thermal neutron absorption probability (P) or the theoretical detection efficiency (η) of h-^{10}BN detectors as a function the detector's layer thickness, *t*, can therefore be expressed as (Maity et al., 2016),

$$\eta = P(t) = 1 - e^{-t/\lambda}, \tag{1}$$

where $\lambda = 47.3\ \mu m$, which is the thermal neutron absorption length in h-^{10}BN. Eq. (1) is plotted in Fig. 9B (Maity et al., 2016), which shows that the efficiency of h-^{10}BN detectors can be increased by simply increasing the layer thickness of h-^{10}BN. This is in sharp contrast to He-3 gas detectors in which the enhancement in the detection sensitivity is achieved through increasing the gas tube diameter, length and gas pressure. Based on the working principles of h-^{10}BN neutron detectors, one can see from Eq. (1) that the key to obtain high intrinsic detection efficiencies is to realize h-^{10}BN epilayers

with large thicknesses. ^{10}BN detectors with a layer thickness of 1λ (~47 μm) and 3λ (~140 μm) would be capable to attain an intrinsic detection efficiency (η) for thermal neutrons of 63% and 95%, respectively. In comparison to ^{3}He gas tubes, 100 μm thick h-^{10}BN detectors are capable of providing an intrinsic detection efficiency of 88% for thermal neutrons, which already exceeds the thermal neutron conversion efficiency of 77% for 1-in. diameter ^{3}He gas tubes pressurized at 4 atm. However, obtaining h-^{10}BN epitaxial layers with thicknesses large than 1λ (>47 μm) is a prerequisite to bring the h-^{10}BN detector technology to a level which can start to compete with ^{3}He gas detector technology. This is a challenging task. Nevertheless, the authors have produced thick h-^{10}BN epilayers by MOCVD. As illustrated in Fig. 1F, the largest thickness attained so far is 200 μm, which is capable to provide an intrinsic detection efficiency of 99% for thermal neutrons. Freestanding epilayers of h-^{10}BN were grown using MOCVD on *c*-plane sapphire substrates. Precursors for ^{10}B and N were 99.9% ^{10}B-enriched trimethylboron and ammonia (NH_3), respectively, and H_2 was used as a carrier gas (Doan et al., 2016a; Grenadier et al., 2019; Maity et al., 2016, 2017a, 2018, 2019a, 2020).

3.2 Requirements in background carrier concentration and dark electrical resistivity

Absorption of a thermal neutron by a ^{10}B atom induces the following nuclear reaction inside h-^{10}BN (Knoll, 1995),

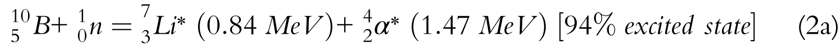

$$ {}^{10}_{5}B + {}^{1}_{0}n = {}^{7}_{3}Li^{*}\ (0.84\ MeV) + {}^{4}_{2}\alpha^{*}\ (1.47\ MeV)\ [94\%\ \textit{excited state}] \quad (2a) $$

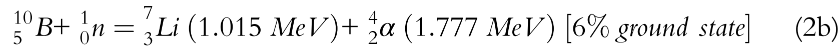

$$ {}^{10}_{5}B + {}^{1}_{0}n = {}^{7}_{3}Li\ (1.015\ MeV) + {}^{4}_{2}\alpha\ (1.777\ MeV)\ [6\%\ \textit{ground state}] \quad (2b) $$

$$ \mathrm{Li}, \alpha \rightarrow \mathrm{N}\ (\mathrm{e}^{-}) + \mathrm{N}\ (\mathrm{h}^{+}) \quad \mathrm{N} \sim 10^{5} \quad (3) $$

The detection of neutrons by a h-^{10}BN detector is accomplished by two sequential processes. The first is the neutron capture of Eq. (2) in which the nuclear reaction creates Li and α daughter particles with large kinetic energies. The second process of Eq. (3) is the subsequent charge carrier generation by Li and α particles and the collection of these electrons (e^{-}) and holes (h^{+}). In contrast to ^{6}LiF (Bellinger et al., 2012a,b, 2014) or ^{10}B (Dahal et al., 2012, 2015; Nikolic et al., 2013; Shao et al., 2013) filled micro-structured semiconductor neutron detectors (MSND), the two sequential processes described by Eqs. (2) and (3) occur in the same h-^{10}BN layer. Therefore, h-10BN detectors are considered as direct conversion neutron

detectors and are capable of providing high charge collection efficiency and hence high detection efficiency for thermal neutrons. On the other hand, the unique properties that set single crystal h-BN material apart from other direct conversion neutron detectors based on amorphous B_4C (Osberg et al., 2006), gadolinium complexes (Losovyj et al., 2007), pyrolytic, polycrystalline BN and alpha rhombahedral boron complexes (Doty, 2004; McGregor et al., 2008; Uher et al., 2007) include: (1) hexagonal BN has a simple crystal structure, which allows for the attainment of single crystalline thin films by epitaxial growth techniques such as MOCVD and (2) materials with single crystalline structure contain few charge traps and allow a rapid sweep-out of the electrons and holes generated by the nuclear reaction. Moreover, due to the high thermal conductivity and high melting point of h-BN, h-BN detectors can withstand extremely high temperatures.

However, to realize h-^{10}BN detectors with high detection efficiency, in addition to the necessary condition of a sufficiently large h-^{10}BN layer thickness, it is also essential to maximize the collection efficiency of charge carriers (electrons and holes) generated by the nuclear reaction described by Eqs. (2) and (3). This demands h-^{10}BN epilayers with high crystalline quality and purity, i.e., low densities of dislocations, native defects and point defects which may act as charge traps. In particular, the detection of neutron signals requires h-^{10}BN epilayers with extremely low background carrier concentrations and high electrical resistivities.

The number of charge carriers generated by each absorbed thermal neutron in Eq. (3) via the nuclear reaction of Eq. (2) can be estimated using the Klein's factor (Klein, 1968):

$$N = \frac{E_r}{3E_g} \sim 1.2 \times 10^5 \text{ (94\% interaction probability)} \tag{4a}$$

$$N = \frac{E_r}{3E_g} \sim 1.4 \times 10^5 \text{ (6\% interaction probability)} \tag{4b}$$

where E_r is the total energy deposited by the daughter particles, $E_r = 2.31$ MeV for the reaction with a 94% probability of Eq. (2a) and $E_r = 2.79$ MeV for the reaction with a 6% probability of Eq. (2b), $E_g \sim 6$ eV. From these, we can estimate the neutron generated carrier density, n_n, in the detector with a detection area of 1 cm^2, thickness of 100 μm, and volume V = 0.01 cm^3 to be.

$$n_n = N/V \approx (1.2 - 1.4) \times 10^7 \text{ cm}^{-3}. \tag{5}$$

This thermal neutron-generated charge carrier density, n_n, represents the size of the electrical signal. In order to detect this signal, the background

carrier concentration, n_o, or the background noise in h-^{10}BN detector itself must be at least one order of magnitude smaller than the neutron generated electrical signal, i.e.,

$$n_o < 10^6\ cm^{-3}. \tag{6}$$

In principle, the intrinsic carrier concentration in h-BN is negligibly small because of its large bandgap of ~6 eV. In practice, however, unintentionally doped h-BN epilayers still contain various deep level native and point defects which not only contribute to the background carrier concentration, but also act as charge traps (Doan et al., 2014b; Du et al., 2015, 2016; Grenadier et al., 2018).

In general, it is notoriously difficult to measure the background carrier concentration in undoped h-BN via traditional techniques such Hall-effect measurement due to its ultrawide bandgap and the deep level nature of native point defects and impurities. The more readily measurable physical parameter is the dark electrical resistivity, ρ, which is directly related to the dark current of a detector. The minimum required electrical resistivity of h-BN can be calculated by knowing the carrier mobility, μ, according to.

$$\rho > \rho 0 = \frac{1}{e n_0 \mu}. \tag{7}$$

Using the measured electron and hole mobility in the lateral direction in a typical thick h-^{10}BN epilayer available today of about $35\,cm^2/cm\cdot s$ (Grenadier et al., 2019), the required minimum dark electrical resistivity of h-^{10}BN detector material for neutron detector fabrication can be determined to be $\rho > \rho_0 = 2 \times 10^{11}\,\Omega\cdot cm$.

The electrical resistivity determines the size of the leakage current, whereas the equivalent noise of the detection circuit increases with increasing leakage current. However, the leakage current is proportional the detection area for a fixed electrical resistivity. The presence of a large level of noise in the detection circuit will have a detrimental effect on detecting the actual neutron signal. Therefore, the presence of a high background noise (or dark count) could limit the ability of scaling up the device size while maintaining an equal level of detection efficiency.

To illustrate the impact of the dark electrical resistivity to the background noise of a neutron detector, Fig. 10A compares the dark current density vs voltage (J_d-V) characteristics of 1 mm × 1 mm detectors fabricated from two different h-^{10}BN samples (Sample A and Sample B) using Ni/Au bilayers as ohmic contacts (Maity et al., 2017b). The J-V characteristics exhibit an excellent ohmic behavior for the more electrically resistive sample

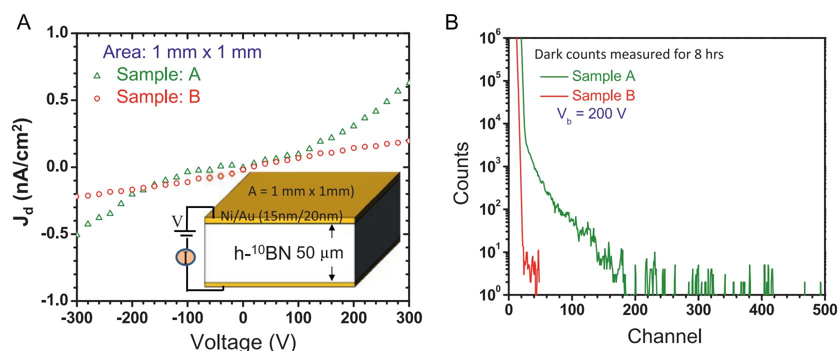

Fig. 10 (A) The leakage (or dark) current density vs voltage (J_d-V) characteristic of two $1 \times 1\,mm^2$ devices fabricated from two h-^{10}BN epilayers, sample A and sample B, produced under different growth conditions using Ni/Au bilayers as ohmic contacts on the top and bottom surfaces. The insets show the schematic of the device structure. (B) Dark counts—Pulse height spectra of $1 \times 1\,mm^2$ detectors fabricated from samples A and B measured under a bias voltage of 200 V for 8 h in absence of any radiation sources. Sample B provides lower leakage current densities and hence lower background counts. *Reproduced from Maity, A., Grenadier, S.J., Li, J., Lin, J.Y., Jiang, H.X., 2017. High-efficiency and high-sensitivity thermal neutron detectors based on hexagonal BN epilayers. Proc. SPIE 10392, Hard X-Ray, Gamma-Ray, and Neutron Detector Physics XIX, 103920L; Copyright (2017) SPIE.*

(Sample B). Fig. 10A also shows that the current density (J_d) of sample B at an applied electric field of 10^5 V/cm (or at a bias voltage of 500 V) is 3×10^{-10} A/cm^2, which is nearly one order of magnitude lower than that of sample A. Fig. 10B compares the pulse height spectra of the same $1\,mm \times 1\,mm$ detectors measured in absence of any radiation source, which were obtained by recording the dark counts for 8 h with the devices biased at 200 V. In practical applications, the detectors are expected to operate for prolonged periods. Therefore, recording the background counts for 8 h corresponds more closely to reality. The pulse height spectra shown in Fig. 10B were recorded by a multichannel analyzer (MCA) in conjunction with a charge sensitive preamplifier and a shaping amplifier. The results clearly revealed that the dark count is almost one order of magnitude lower for the detector fabricated from sample B than the detector fabricated from sample A, due to the fact that Sample B has a higher electrical resistivity (and hence lower dark currents) than Sample A.

The presence of a high noise level will alter the low-level discriminator threshold setting on the detection electronics for pulse height analysis, which could exclude a fraction of the actual neutron counts from being detected

and thereby decrease the detection efficiency. As the bandgap of h-BN is more than 6 eV (Arnaud et al., 2006; Cao et al., 2013; Doan et al., 2016b; Huang et al., 2012; Majety et al., 2012b; Wirtz et al., 2006), intrinsic h-BN epilayers are expected to possess an electrical resistivity exceeding $10^{20}\,\Omega\cdot$cm. However, the highest resistivity of unintentionally doped h-BN epilayers produced so far is about $5\times10^{14}\,\Omega\cdot$cm (Doan et al., 2014a, 2016a; Grenadier et al., 2019; Maity et al., 2016, 2017a, 2018, 2019a, 2020), implying that a significant improvement is still anticipated through the optimization of epitaxial growth processes in order to eliminate undesirable defects and impurities.

3.3 Necessary conditions for attaining high charge collection efficiencies

As shown in Fig. 1, we have successfully produced freestanding and single crystal h-^{10}BN epilayer wafers of 4-in. in diameter with large thicknesses (up to 200 μm) (Grenadier et al., 2019; Maity et al., 2016, 2017a, 2018, 2019a, 2020). As such, photoconductive-type of neutron detectors in a vertical geometry, as that schematically shown in Fig. 11A, have been constructed from these freestanding wafers (Maity et al., 2016, 2017a, 2018). The fabrication processes for vertical detectors include dicing h-^{10}BN wafers into desired shapes and dimensions followed by top and bottom contact deposition. The electrical contacts on h-BN films and the electrodes must be sufficiently electrically conducting so that the free carriers generated by the nuclear reaction are not blocked from flowing into the external measurement circuit. Hence, low-resistance contacts are needed. This will ensure that the electric field applied will be across the h-BN

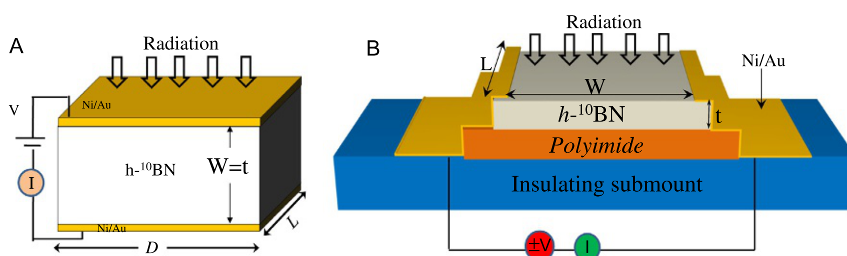

Fig. 11 Schematics of h-^{10}BN detector architecture designs: (A) a vertical detector and (B) a lateral detector. For the same detection area and detector thickness, the lateral detector design provides higher carrier mobility in the lateral direction due to the layered structure of h-BN. This structure also features lower device capacitance and surface recombination field due to a reduction in the metal/h-^{10}BN contact area.

detectors, as needed to sweep out the free charge carriers. Vertical neutron detectors of $1\,\mathrm{mm} \times 1\,\mathrm{mm}$ and $3\,\mathrm{mm} \times 3\,\mathrm{mm}$ have been fabricated from $50\,\mu\mathrm{m}$ thick h-^{10}BN epilayers, which have demonstrated record high thermal neutron detection efficiencies among solid-state neutron detectors and a gamma rejection ratio (GRR) of better than 10^{-6} (Maity et al., 2016, 2017a, 2018). However, the detection sensitivities of these vertical detectors have been limited due to the technical challenges in scaling up the detection area.

The neutron count rate (C_R) observed by a detector (or the sensitivity of a detector) is proportional to its detection efficiency (η) and detection area (A), $C_R \propto \eta A$. Thus, scaling up the detector size while maintaining a high detection efficiency is critical, but also challenging. This is because the total detection efficiency not only depends on the epilayer thickness, but also on the charge collection efficiency. The dark current (or the leakage current), the capacitance, the number of dislocations/defects/carrier traps and the surface recombination field all increase with an increase in detector area, all of which can have a profound effect on charge collection efficiency. It is known that the equivalent noise charge in a simple CR-RC shaper at a fixed integration and differentiation time constant τ_c can be written as (Spieler and Haller, 1985),

$$\left\langle Q_n^2 \right\rangle = 0.924 \left[2eI_d\tau_c + \frac{4K_BT}{R_b}\tau_c + e_n^2\frac{C^2}{\tau_c} \right]. \tag{8}$$

The "shot noise" in the first term of Eq. (8) increases with the detector's dark current I_d, which is proportional the device area (A). The second term is the "thermal noise" contributed from the bias resistor R_b. K_B is the Boltzmann's constant and T is the operating temperature. The last term in Eq. (8) depends on the equivalent input noise of the amplifier with a spectral density e_n and equivalent input capacitance C. Overall, the electronic noise increases linearly with the dark current (I_d) and quadratically with capacitance (C) (Spieler and Haller, 1985).

To overcome to some extent these challenges, a lateral detector scheme has been developed to scale up the detector size, as schematically shown in Fig. 11B (Grenadier et al., 2019; Maity et al., 2019a, 2020) to reduce the metal contact area and hence the associated values of capacitance and surface recombination field. By inspecting the device configurations of Fig. 11A and B, for the same detection area and the detector thickness, the device capacitance in the lateral configuration is reduced by about two orders of magnitude compared to the vertical detector. Moreover, the lateral mobility (μ) of

charge carriers of h-BN in the *c*-plane is expected to be much higher than the vertical mobility along the c-axis due to the conduction anisotropy in layered semiconductors (Gallos et al., 1994). The fabrication processes for lateral detectors include the following steps: (1) dicing ^{10}BN wafers into detector strips (with a width W and length L), (2) combine multiple strips to form a large size photoconductive-type lateral detector; (3) mount detector strips on a highly electrically resistive submount such as sapphire using a highly resistive adhesive material; (4) a mask can be used to deposit ohmic contacts consisting of a bi-layer of Ni (100 nm)/Au (40 nm) on the clipped edges of the h-^{10}BN strips using e-beam evaporation, leaving around $\sim$100 μm of metal covering on the edges (Grenadier et al., 2019; Maity et al., 2019a, 2020). As of this writing, the largest h-^{10}BN detector size attained by our group so far is 1 cm^2. The 1 cm^2 detector utilizing a lateral geometry has demonstrated an unprecedented detection efficiency of 59% (Maity et al., 2020).

It is critically important to understand the charge collection process in Eq. (3). After charge carrier generation, with the aid of an external applied electric field, these electrons and holes move across the detector toward the anode and cathode and are then collected through the electrodes to serve as the detection signal of an absorbed thermal neutron. Most of the neutron-generated charge carriers, electrons (e^-) and holes (h^+) inside a detector can be collected when the recombination time (τ) is much greater than the transit time (τ_t), $\tau \gg \tau_t$, [or the charge carrier drift length ($= \mu\tau E$) $\gg$ the carrier transit distance (W)], (where $\tau_t = W/\mu E$, $E = V/W$),

$$\mu\tau E \gg W, \text{ or} \tag{9a}$$

$$W^2 \ll V\mu\tau \tag{9b}$$

where μ is the charge carrier mobility, τ is the mean lifetime of charge carriers, and E (V) is the applied electric field (bias voltage). In Eq. (9), W is the carrier transit distance or the distance between the two electrodes. In the vertical detectors, W is the thickness of the detector. In the lateral detectors, W is the detector strip width. Eq. (9) implies that the required applied electric field to attain the same charge collection efficiency is inversely proportional to the carrier mobility-lifetime product ($\mu\tau$) of the detector material for a given W, whereas the quantity of $\mu\tau$ determines the conduction capability of radiation-generated carriers and is strongly influenced by the overall material quality. On the other hand, at a given bias voltage, the width of the detector strip of a lateral detector (W) (and hence the detection area) is

limited by the quantity of $\mu\tau$. For instance, assuming the measured values $\mu_e\tau_e = \mu_h\tau_h = 4 \times 10^{-5}$ cm^2/V and intended bias voltage is 500 V, the detector strip width should be made to be less than 1.4 mm ($W \leq \sqrt{V\mu\tau} = \sqrt{500 \text{ x } 4 \text{ x } 10 - 5} \approx 0.14$ cm) in order to ensure a high charge collection efficiency.

Another condition for attaining a high charge collection efficiency is $\frac{sW}{\mu V} \ll 1$, which is governed by the surface recombination velocities, s. By defining s/μ as the "surface recombination field", E_S, we can rewrite this condition as (Maity et al., 2019b),

$$\frac{s/\mu}{V/W} = \frac{Es}{E} \ll 1, \tag{10}$$

where $E\left(= \frac{V}{W}\right)$ denotes the external applied electric field. Introducing E_S is useful for understanding the effects of surface recombination on charge collection efficiency. The ratio of surface recombination velocity to mobility is not only a measure of an "effective electric field" at the surfaces, but it also provides a direct way for quantifying the necessary charge collection condition with respect to the applied electric field, that is $\frac{Es}{E} \ll 1$. In other words, other than the charge transport processes occurring in the bulk as described by Eq. (9), radiation-generated charge carriers must also overcome the surface trap induced potential barriers or surface recombination fields at the detector surfaces in order to be extracted by the electrodes. As such, the external applied electric field must be much greater than the surface recombination field, $E \gg E_S$, in order to effectively sweep out charge carriers. Comparing the device configurations of Fig. 11A and B, the surface recombination field (E_S) in the lateral detector is reduced by about one order of magnitude over that in the vertical detector with the same detection area (Maity et al., 2019b).

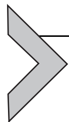

4. Vertical electrical transport properties and parameters

4.1 Carrier mobility-lifetime product and surface recombination field characterization

As shown in Eqs. (9) and (10), the charge carrier mobility-lifetime product (μτ) and surface recombination field E_S (= s/μ) are two of the most important material parameters for determining the charge collection efficiency of

h-BN detectors. In h-BN, due to its layered structure, the optical absorption length of the above bandgap photons is only about 14.5 nm (Li et al., 2012). This property enables us to characterize electrical transport properties for photogenerated electrons and holes separately, as schematically illustrated in the middle inset of Fig. 12. Depending upon the polarity of the illuminated surface, a specific charge carrier type (hole or electron) can be selected for charge transport in the vertical direction. The experimental configuration shown in the top (bottom) inset of Fig. 12, holes (electrons) are rapidly extracted by the illuminated top cathode (anode). This allows for the transport property of electrons (holes) to be probed (Maity et al., 2016, 2017a, 2018, 2019a). To obtain the photocurrent-voltage characteristics under UV excitation, 1 mm × 1 mm photoconductive-type detectors were fabricated from h-^{10}BN epilayers of 50 μm in thickness. UV-transparent bilayers of Ni (10 nm)/Au (20 nm) were deposited on the top and bottom surfaces of the h-^{10}BN epilayers by e-beam evaporation to form ohmic contacts.

The photocurrent-voltage characteristics under UV excitation can be utilized to extract $\mu\tau$ and E_S using the classical Many's equation for insulating semiconductors by taking into consideration both the effects of surface recombination and bulk trapping (Many, 1965),

$$I_i(V) = I_{0,i}\left[\eta_{c,i}(V)\right],$$
$$\eta_{c,i}(V) = \left[\frac{V\mu_i\tau_i\left(1 - e^{-\frac{W^2}{V\mu_i\tau_i}}\right)}{W^2\left(1 + \frac{s_i W}{\mu_i V}\right)}\right], (i = e, h). \tag{11}$$

Here $\eta_c(V)$ defines as the charge collection efficiency at an external bias voltage (V) applied between the two electrodes, I_0 is the saturation current, $\mu_h\tau_h$ ($\mu_e\tau_e$) and s_h (s_e) denote, respectively, the mobility-lifetime product and surface recombination velocity for holes (electrons), and W is the thickness of the detector (or the carrier transit length). In order to achieve a high charge collection efficiency, $\eta_c(V)$, the two conditions stated in Eqs. (9) and (10) must be satisfied, or equivalently both the numerator term of $\frac{V\mu\tau}{W^2}\left(1 - e^{-\frac{W^2}{V\mu\tau}}\right)$ and the denominator term of $\frac{1}{\left(1+\frac{sW}{\mu V}\right)}$ in Eq. (11) should approach to 100%, i.e.,

(a) $\frac{V\mu\tau}{W^2}\left(1 - e^{-\frac{W^2}{V\mu\tau}}\right) \rightarrow 1$ or $\frac{W^2}{V\mu\tau}\left(= \frac{W}{\mu\tau E}\right) \ll 1$, which simply states that the charge carrier drift length ($= \mu\tau E$) needs to be much larger than the carrier transit distance, W. This condition is predominantly determined

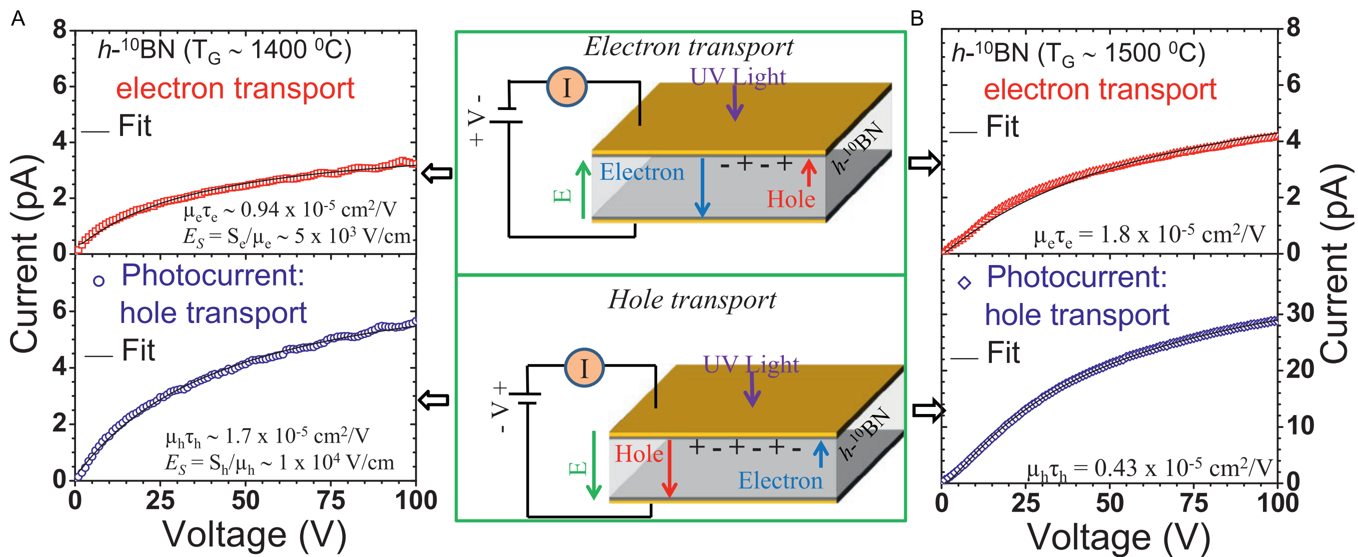

Fig. 12 (A) Photocurrent-voltage characteristics of freestanding *h*-BN samples grown at (A) ∼1400 °C and (B) ∼1500 °C. The solid curves are least squares fittings using Eq. (11), which reveal that $\mu_h\tau_h > \mu_e\tau_e$ for the sample grown at ∼1400 °C and $\mu_e\tau_e > \mu_h\tau_h$ for the sample grown at ∼1500 °C. The inset in the middle panel shows the experimental geometries which enable the characterization of the electron and hole transport properties separately. *Reproduced from Grenadier, S.J., Maity, A., Li, J., Lin, J.Y., Jiang, H.X., 2018. Origin and roles of oxygen impurities in hexagonal boron nitride epilayers. Appl. Phys. Lett. 112, 162103; Copyright (2018) AIP Publishing.*

by the bulk trapping properties as represented by the numerator of Eq. (11), which provide a useful guidance on the achievable η_c at a certain bias voltage for a given material (with a fixed $\mu\tau$ product value).

(b) $\frac{1}{\left(1+\frac{sW}{\mu V}\right)} \to 1$ or $\frac{sW}{\mu V}\left(=\frac{s/\mu}{V/W}=\frac{E_s}{E}\right) \ll 1$, which implies that the external applied electric field must be greater than the surface recombination field, $E \gg E_s$, in order to effectively sweep out charge carriers (Maity et al., 2019b). This condition is dominated by the surface effects described in the denominator of Eq. (11) and represents attainable η_c at a certain bias voltage at a given surface condition (or a surface recombination field).

Fig. 12A shows the photocurrent-voltage characteristics of a 1 mm × 1 mm device fabricated from a 50 μm thick h-^{10}BN epilayer grown at a temperature of 1400 °C. Fitting the measured I-V curves under UV photoexcitation with Eq. (11) yielding values of $\mu_h\tau_h$ and $\mu_e\tau_e$ for holes and electrons of 1.7×10^{-5} and 0.94×10^{-5} cm^2/V, respectively and values of E_s (= s/μ) for holes and electrons of 1×10^4 V/cm and ~5×10^3 V/cm, respectively. It is interesting to note from Fig. 12A that the $\mu\tau$ product for holes is greater than that of electrons for this 50 μm thick h-^{10}BN epilayer grown at a temperature of 1400 °C, $\mu_h\tau_h$ (1.7×10^{-5} cm^2/V) > $\mu_e\tau_e$ (0.94×10^{-5} cm^2/V). This implies that holes act more like majority carriers in h-^{10}BN epilayers grown at about 1400 °C or below. This observation is consistent with the results shown in Fig. 5, which revealed that typical unintentionally dope h-BN epilayers exhibit a weak "p-type" character.

Among all the MOCVD growth parameters, it was found that the growth temperature has the strongest influence on the electrical transport properties of h-BN (Grenadier et al., 2018). In h-BN epilayers grown at relatively low temperatures (T_G < 1400 °C), holes behave as majority carriers. However, for materials grown at relatively high temperatures (T_G > 1500 °C), h-BN epilayers exhibit an n-type character (Grenadier et al., 2018). This dramatic change in carrier conduction type is illustrated in Fig. 12B, which shows the measured I-V characteristics under UV excitation for a 50 μm thick h-^{10}BN epilayer grown at a temperature of ~1500 °C. Fitting the measured photocurrents with Eq. (11) yields values of $\mu_e\tau_e$ (1.8×10^{-5} cm^2/V) > $\mu_h\tau_h$ (0.43×10^{-5} cm^2/V) for the epilayer grown at a temperature of 1500 °C. We attribute this change in the conduction type from p-type to n-type to the use of sapphire substrates and the incorporation of more oxygen related defects in samples grown at higher temperatures (Grenadier et al., 2018; Maity et al., 2018). In h-BN, oxygen

impurities occupying nitrogen sites (O_N) form donors (Weston et al., 2018) and their presence makes the sample behavior more n-type. These oxygen impurities were diffused from the sapphire substrate during MOCVD growth with the diffusion rate increasing exponentially with increasing the growth temperature.

4.2 Charge collection efficiency characterization

Fig. 13A plots the calculated values of $\frac{W^2}{V\mu\tau}$ and $\frac{s/W}{\mu V}$ as functions of the applied voltage (V) up to 200 V for several different values of $\mu\tau$ products between 10^{-6} and 10^{-4} cm^2/V and s/μ between 10^2 and 10^3 V/cm for $W = 50\,\mu$m. The values of $\frac{W^2}{V\mu\tau}$ shown in the top panel of Fig. 13A are predominantly determined by the bulk trapping as represented by the numerator of Eq. (11). The values of $\frac{s/\mu}{V/W}$ shown in the bottom panel Fig. 13A are

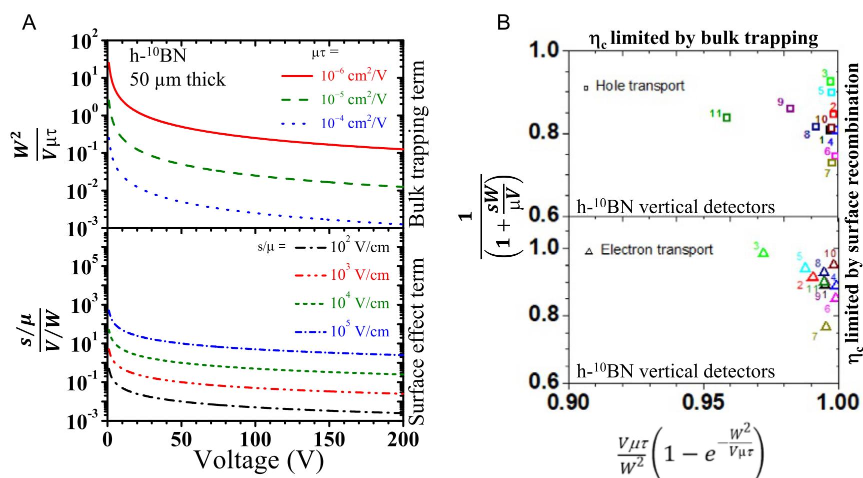

Fig. 13 (A) Plot of bias voltage (V) dependence of $\frac{W^2}{V\mu\tau}$ (top) for $\mu\tau$ products of 10^{-6}, 10^{-5}, and 10^{-4} cm^2/V and $\frac{sW}{\mu V}$ $\left(= \frac{s/\mu}{V/W}\right)$ (bottom) for s/μ value of 10^2, 10^3, 10^4, and 10^5 V/cm for 50 μm thick h-BN vertical detectors. (B) Plot of the denominator term of $1/\left(1+\frac{sW}{\mu V}\right)$ vs the numerator term of $\frac{V\mu\tau}{W2}\left(1-e^{-\frac{W2}{V\mu\tau}}\right)$ in Eq. (11) for photo-excited hole and electron transport, using the measured $\mu\tau$ product and s/μ values obtained from a set of 11 vertical neutron detectors with a detection area of 1 mm × 1 mm fabricated from different h-BN samples. *Reproduced from Maity, A., Grenadier, S.J., Li, J., Lin, J.Y., Jiang, H.X., 2019. Effects of surface recombination on the charge collection in h-BN neutron detectors. J. Appl. Phys. 125, 104501; Copyright (2019) AIP Publishing.*

dominated by the surface effects contained in the denominator of Eq. (11). To achieve a high charge collection efficiency (η_c), both conditions of $\frac{W^2}{V\mu\tau} \ll 1$ and $\frac{s/\mu}{V/W} \ll 1$ need to be satisfied.

At the present stage of material development, most thick h-^{10}BN epilayers grown by MOCVD possess vertical $\mu\tau$ products of about 10^{-5} cm^2/V or greater (Maity et al., 2017a, 2018, 2019b). As shown in the top panel of Fig. 13A, at a bias voltage of 200 V, the condition for overcoming the effect of bulk trapping stated in Eq. (9), $\frac{W^2}{V\mu\tau} \ll 1$, is already satisfied with $\frac{W^2}{V\mu\tau} \sim 0.01$ for detectors with a thickness of 50 μm (and $\frac{W^2}{V\mu\tau} \sim 0.05$ for detectors with a thickness of 100 μm). However, the measured values of E_S (= s/μ) of thick h-^{10}BN samples are between 10^3 and 10^4 V/cm, providing values of $\frac{sW}{\mu V}\left(=\frac{s/\mu}{V/W}=\frac{E_S}{E}\right) \sim 25\%$ at a bias voltage of 200 V, as depicted in the bottom panel of Fig. 13A (Maity et al., 2019b), which is less than desirable.

To further illuminate this point, in Fig. 13B, the values of the numerator term of Eq. (11), $\frac{V\mu\tau}{W^2}\left(1-e^{-\frac{W^2}{V\mu\tau}}\right)$, are plotted against those of the denominator term of Eq. (11), $\frac{1}{\left(1+\frac{sW}{\mu V}\right)}$, using the measured $\mu\tau$ product and s/μ values obtained from a set of 11 vertical neutron detectors fabricated from various h-^{10}BN samples (Maity et al., 2019b). Ideally, both terms of $\frac{V\mu\tau}{W^2}\left(1-e^{-\frac{W^2}{V\mu\tau}}\right)$ and $\frac{1}{\left(1+\frac{sW}{\mu V}\right)}$ need to approach to 100% in order to achieve a perfect charge collection efficiency, η_c. The majority of detectors have $\mu\tau$ product values of $\sim 10^{-5}$ cm^2/V or greater and values of $\frac{V\mu\tau}{W^2}\left(1-e^{-\frac{W^2}{V\mu\tau}}\right)$ $\sim$99% or greater, as shown in Fig. 13B. This means that the charge collection efficiency already approaches 99% if we consider the bulk transport alone. Therefore, further improvement in $\mu\tau$ products will not significantly improve the charge collection efficiency as the values of the numerator term of $\frac{V\mu\tau}{W^2}\left(1-e^{-\frac{W^2}{V\mu\tau}}\right)$ in Eq. (11) for most of the vertical detectors is already approaching 99%. On the other hand, the values of the surface related term of the denominator of Eq. (11), $1/\left(1+\frac{sW}{\mu V}\right)$, have a much larger variation, ranging from 70% to 90%. For instance, for device #7 in Fig. 13B, the measured values of the charge collection efficiencies limited by the bulk trapping, $\frac{V\mu\tau}{W^2}\left(1-e^{-\frac{W^2}{V\mu\tau}}\right)$, are 99.8% and 99.6% at a bias voltage of 200 V for holes and

electrons, respectively. However, the measured "surface recombination fields" for the same device are 2.1×10^4 and 1.8×10^4 V/cm for holes and electrons, respectively, providing the charge collection efficiencies limited by the surface recombination effect, $1/\left(1+\frac{sW}{\mu V}\right)$, of 72.7 and 76.5% at a bias voltage of 200 V for holes and electrons, respectively (Maity et al., 2019b). These lead to overall charge collection efficiencies for holes and electrons in device #7 of 72.6% and 76.1%, respectively. Therefore, the results again confirm that the overall charge collection efficiencies are largely limited by the surface recombination fields in vertical detectors. Consequently, minimizing the surface recombination velocities or equivalently minimizing the ratio of E_S/E_a is necessary to further improve the charge collection efficiency. On the other hand, increasing the applied voltage (or E_a) can help to thrust the charge carriers to overcome the surface recombination fields and push the term of $1/\left(1+\frac{s_i L}{\mu_i V}\right)$ close to 100%, but is less advantageous for practical applications. Furthermore, it was shown that the "surface recombination fields", s/μ, appear to increase with increasing the detector size (Maity et al., 2019b). Therefore, the surface recombination field represents one of the major challenges to scale up to large detection areas for vertical detectors.

Inspecting the necessary conditions for attaining high charge collection efficiencies (η_c) in Eqs. (9)–(11), it can be seen that enhancing the carrier mobility (μ) will be most effective for improving η_c because increasing μ would not only increase the charge carrier drift length ($= \mu\tau E$), but also decrease the surface recombination field, E_s ($=$ s/μ). However, this would demand further optimization in MOCVD growth processes for obtaining h-BN epilayers with improved crystalline quality and purity. For benchmarking purposes, it is useful to compare the key transport parameters of μτ products measured for the h-^{10}BN epilayers currently under development for neutron detectors to those of more well-known CdTe and CdZnTe semiconductor materials for gamma detectors. While the measured value of μτ for holes in h-^{10}BN is comparable to those in CdTe and CdZnTe gamma detector materials, the μτ value for electrons is about one order of magnitude lower than those in CdTe and CdZnTe (Takahashi and Watanabe, 2001).

4.3 Thermal neutron detection efficiency characterization

As schematically shown in Fig. 14A, a Californium-252 (^{252}Cf) neutron source with a radioactivity of 0.77 mCi ($\sim 3.29 \times 10^6$ n/s) moderated by a 1-in.-thick high density polyethylene HDPE moderator was constructed

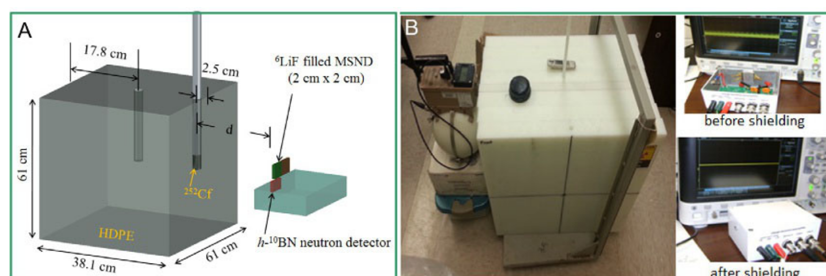

Fig. 14 (A) Schematic diagram of a thermal neutron source constructed from a ^{252}Cf source moderated by a high-density polyethylene (HDPE) for characterizing the thermal neutron detection efficiencies of h-^{10}BN detectors. (B) Photos of the actual neutron source setup (left) and the associated electronics including a multi-channel analyzer (MCA) for pulse height spectra measurements (right). *Reproduced from Maity, A., Doan, T.C., Li, J., Lin, J.Y., Jiang, H.X., 2016. Realization of highly efficient hexagonal boron nitride neutron detectors. Appl. Phys. Lett. 109, 072101; Copyright (2016) AIP Publishing.*

based on a previous work (Clinton, 2011) and used to provide thermal neutrons as described in earlier works (Ahmed et al., 2017; Doan et al., 2014a, 2016a; Grenadier et al., 2019; Maity et al., 2016, 2017a, 2018, 2019a, 2020). Photos of the actual neutron source setup and the associated electronics including a multi-channel analyzer (MCA Amptek 8000D) for pulse height spectra measurements are shown in Fig. 14B. The detection electronics were commercially obtained from Cremat Inc. and included a charge sensitive preamplifier and a Gaussian-shaping amplifier. A Gaussian shaped pulse was fed into the MCA to obtain the pulse height spectrum of the reaction conceived inside the *h*-BN detector. Analog amplifiers were shielded from electronic noise inside an aluminum box along with the detector. A preamplifier (model CR-110) was chosen for maximum amplification of the signal with minimum noise induction. A Gaussian shaping amplifier (model CR-200) with a 2 μs shaping time (FWHM 4.7 μs) was used for further amplification and pulse shape optimization. The experiment was set up in such a way that the distance between the detector and ^{252}Cf source was d cm (or $d - 2.5$ cm from the front surface of the moderator) as depicted in Fig. 14A.

Neutrons are counted one at a time due to the very low flux of incident neutrons on the detector compared to the response time of the detection system with a FWHM of the output Gaussian pulse of 4.7 μs. Daughter (Li and α) particles produced from the nuclear reaction of Eq. (2) travel inside the *h*-BN film and subsequently generate electron-hole clouds on their way. Li and α particles both have short ranges (about 2 μm for Li and 5 μm for α) (Doty, 2004; Knoll, 1995) in *h*-BN compared to device

thickness and therefore deposit all their energies inside the *h*-BN. When the conditions for charge collection of Eqs. (9) and (10) are satisfied, most charge carriers are collected on the electrodes within a very short time, which is integrated in the charge sensitive preamplifier generating a voltage pulse at the output. This voltage pulse is then amplified and shaped in the Gaussian shaping amplifier. Each pulse therefore corresponds to one neutron absorbed and is placed at a certain channel by the MCA.

The total neutron counts detected by a h-^{10}BN detector were obtained by integrating the spectrum beyond the highest channel of dark response, which effectively acted as a low-level discriminator (LLD). Thermal neutron detection efficiency of the *h*-^{10}BN detector was calibrated against a commercially purchased ^{6}LiF filled micro-structured semiconductor neutron detector (MSND) from Radiation Detection Technologies, Inc. This MSND (Domino™ V4 model D411S-30-D0010-V4) has a built-in circuit which outputs 10 V TTL pulses. Furthermore, the circuit for the MSND also includes a built-in LLD which eliminates any background counts. The MSND detector was constructed by combining four 1 cm^2 detectors with a specified detection efficiency of 30 (±1) % for thermal neutrons. By placing the MSND at the same position as the h-^{10}BN detector and knowing its detection efficiency (30%) and detection area (4 cm^2), the thermal neutron detection efficiency of the h-^{10}BN detector can be obtained by comparing the ratio of the count rates per unit area among both the h-^{10}BN and MSND detectors.

The pulse height spectra in response to thermal neutrons of representative $1 \times 1\,mm^2$ and $3 \times 3\,mm^2$ vertical detectors were recorded at a bias voltage of 200 V for 15 min and are shown in Fig. 15A and B. The corresponding "dark" responses were also measured without any radiation exposure under the same conditions. Gamma exposure from Cesium-137 (^{137}Cs) confirmed the unresponsiveness of *h*-BN detectors to gamma photons (Maity et al., 2016). The results revealed that the highest detection efficiency attained by the $1 \times 1\,mm^2$ detector is about 58%, whereas that attained by the $3 \times 3\,mm^2$ detector is about 53% at a bias voltage of $V_b = 200\,V$ (or $E = 4 \times 10^4\,V/cm$) (Maity et al., 2017a, 2018). As indicated in Fig. 15C, the dark current densities for both $1 \times 1\,mm^2$ and $3 \times 3\,mm^2$ detectors are comparable. However, the measured detection efficiency of the $3 \times 3\,mm^2$ detector is reduced compared to that of the $1\,mm^2$ detector. We believe that this is primarily due to an increased surface recombination field, E_s, with an increase in the detection area. This speculation is supported by the results shown in Fig. 15D, which revealed that E_s values for both

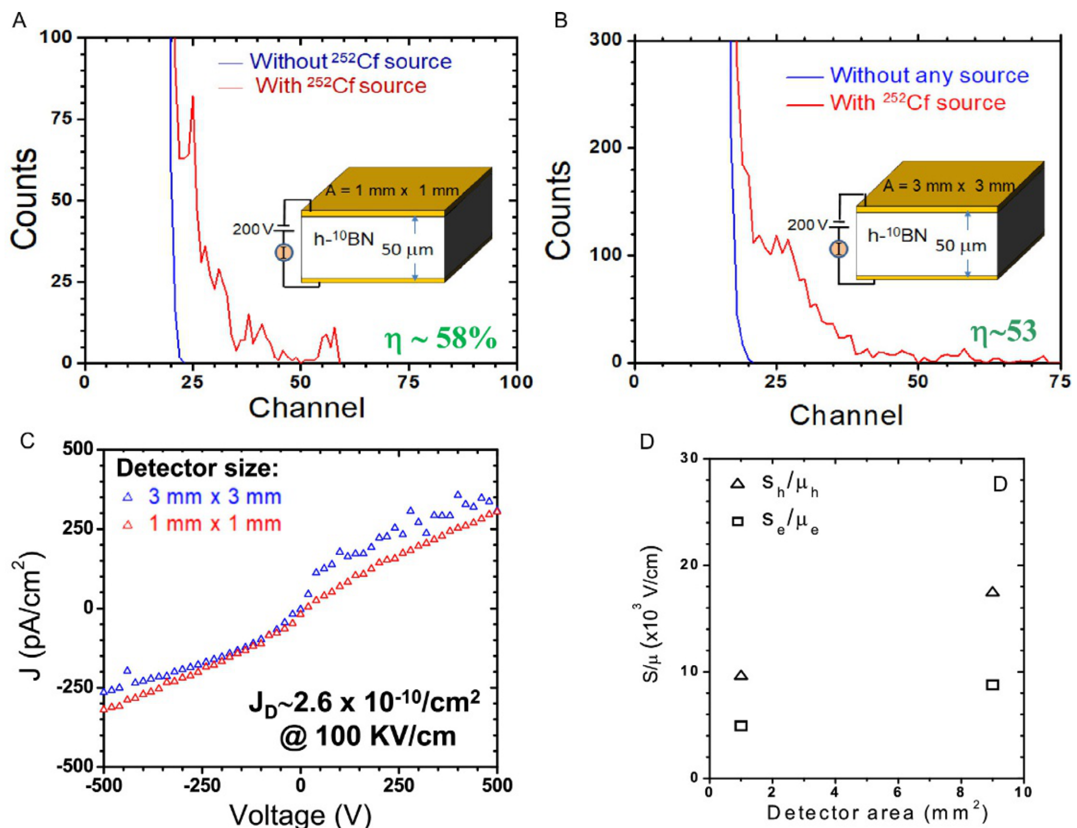

Fig. 15 See figure legend on next page.

electrons and holes are increased in larger detectors (Maity et al., 2019b). The increase in E_s values impacted the charge collection efficiencies in larger detectors. Thus, the thermal neutron detection efficiency characterization results shown in Fig. 15 again suggested that the surface recombination field is one of the primary factors that limits the ability to scale up to large detection area using the vertical detector architecture (Maity et al., 2019b). Moreover, the device capacitance also increases with an increase of the device size, which further limits the ability to scale up the detector size in the vertical geometry. It was found that the typical detection efficiency is below 15% for vertical detector size $>25\,\text{mm}^2$.

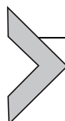

5. Lateral electrical transport properties and parameters

5.1 Lateral charge carrier transport properties probed by time-of-flight technique

Because h-BN has a very large energy bandgap and hence high electrical resistivity, it is very challenging to separately characterize its charge carrier drift mobility (μ) and lifetime (τ). However, μ and τ are considered two of the most fundamental parameters which are directly related to the overall performance of its associated electronic and detector devices. Hall-effect measurements have been only possible at high temperatures for h-BN, as shown in Fig. 5 (Doan et al., 2014b). Moreover, the classical Hall-effect measurement can only provide the mobility of one type of charge carrier (electrons or holes). On the other hand, the combined mobility-lifetime

Fig. 15 (A) The nuclear reaction pulse height spectrum of a 1 mm × 1 mm h-^{10}BN detector with the device configuration shown in the inset. (B) The nuclear reaction pulse height spectrum of a 3 mm × 3 mm h-^{10}BN detector with the device configuration shown in the inset. The neutron response was measured by placing the detector at a distance of d = 30 cm away from the ^{252}Cf source moderated by a one-inch-thick high-density polyethylene (HDPE) moderator. These measurements were taken at a bias voltage of 200 V for 15 min. (C) Dark current density J-V characteristics measured for the 1 mm × 1 mm and 3 mm × 3 mm detectors. (D) Measured surface recombination fields for holes and electrons in the 1 mm × 1 mm and 3 mm × 3 mm detectors. *Reproduced from Maity, A., Grenadier, S.J., Li, J., Lin, J.Y., Jiang, H.X., 2017. Toward achieving flexible and high sensitivity hexagonal boron nitride neutron detectors. Appl. Phys. Lett. 111, 033507; Copyright (2017) AIP Publishing; Maity, A., Grenadier, S.J., Li, J., Lin, J.Y., Jiang, H.X., 2018. Hexagonal boron nitride neutron detectors with high detection efficiencies. J. Appl. Phys. 123, 044501; Copyright (2018) AIP Publishing; Maity, A., Grenadier, S.J., Li, J., Lin, J.Y., Jiang, H.X., 2019. Effects of surface recombination on the charge collection in h-BN neutron detectors. J. Appl. Phys. 125, 104501; Copyright (2019) AIP Publishing.*

($\mu\tau$) product can be obtained by measuring and analyzing the photocurrent-voltage characteristics using Eq. (11) (Many, 1965).

Time-of-flight (TOF) is a useful technique for the exploration of the electrical transport properties of semiconductor materials (Chen et al., 2000; Guan et al., 2000; Isberg et al., 2002; Lebedev et al., 1997), including freestanding h-^{10}BN epilayers (Grenadier et al., 2019). The schematic diagram of the h-^{10}BN sample used for TOF characterization is shown in the top panels of Fig. 16 (Grenadier et al., 2019). A pulsed excimer laser with a lasing wavelength of 193 nm and a pulse width of 20 ns was used to generate the excitation light pulses at a repetition rate of 1 Hz. A metal slit was used to allow light to enter and illuminate only near one of the metal contacts of the structure. One type for the photogenerated charge carriers are immediately collected at the charge generating electrode, whereas the other type of photogenerated charge carriers are drifted across the material with the aid of an applied electric field and collected by the opposite electrode at a delayed time, τ_t, known as the transit time. With the known electric field strength E, transit time τ_t and drift distance W, the drift mobility of the charge carrier can be determined by,

$$\mu = \frac{W}{E \cdot \tau_t}, \tag{12}$$

whereas the mobilities of electrons and holes can be measured separately by changing the polarity of the applied electric field, as illustrated in the top panels of Fig. 16 (Grenadier et al., 2019).

A charge sensitive preamplifier in conjunction with a shaping amplifier instead of a simple current sensing resistor was used in the TOF setup to enhance the photo-generated charge carrier signals from the highly resistive h-^{10}BN epilayers (Grenadier et al., 2019). Waveforms were measured under different bias voltages (V) between 50 and 150 V, corresponding to electric field strengths (E) between 250 and 750 V/cm with a distance of 2 mm between the two electrodes. The transit time was obtained by performing a Lorentzian fit around the second peak and extracting the location of the peak's center. Examples of this fitting at an applied bias voltage of 90 V are shown in Fig. 16A and B for electron and hole transport, respectively. The insets of Fig. 16A and B show plots of measured transit time vs applied electric field E for electrons and holes, respectively. It is clear that the transit time for the drifted charge carriers decreases with increasing V or E. By dividing the transit distance (W = 2 mm) by the transit time of the drifted carriers, the carrier velocity vs E for electrons and holes can be obtained,

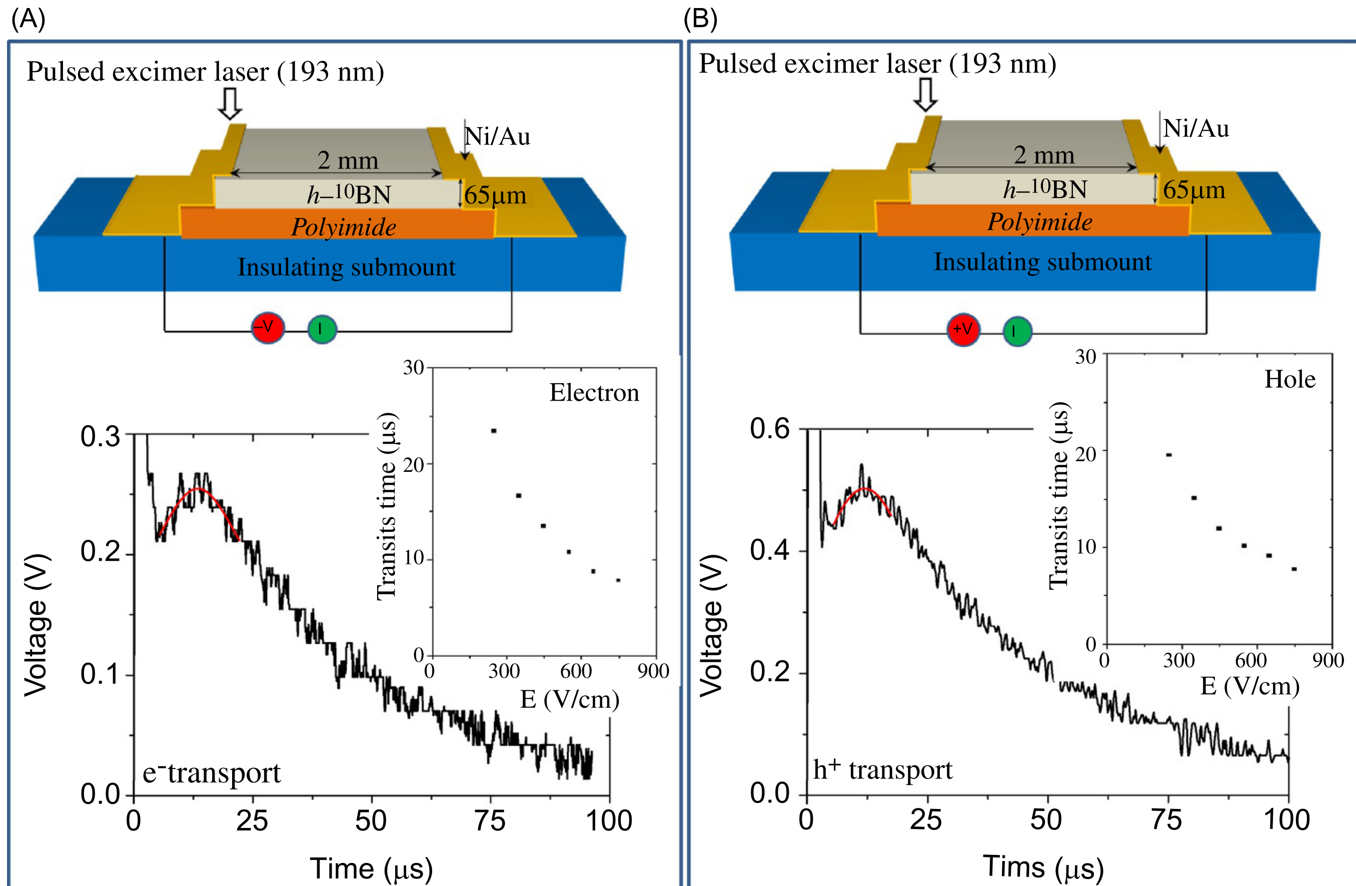

Fig. 16 See figure legend on opposite page.

as shown in Fig. 17A. The slope of the linear fit of this data provides the mobility of the drifted carriers. From this, drift mobilities of $\mu_e = 34.2\,cm^2/Vs$ for electrons and $\mu_h = 35.5\,cm^2/Vs$ for holes have been obtained (Grenadier et al., 2019). The mobilities of electrons and holes in the lateral direction in h-BN are expected to be comparable because the effective masses of electrons and holes in single sheet h-BN are equal (Cao et al., 2013; Semenoff, 1984). Moreover, As shown in Fig. 17B, the measured carrier lifetime for holes was $\tau_h = 9.1\,\mu s$, whereas the data points collected for electron transport exhibited two slopes, indicating the possible presence of electrons at two different energy levels for photo-excitation, one with a lifetime of $\tau_{e1} = 10.8\,\mu s$ and the other with a lifetime of $\tau_{e2} = 23.3\,\mu s$ (Grenadier et al., 2019).

Fig. 17C plots the photocurrent-voltage characteristics measured for the same sample under UV excitation for electrons and holes. Fitting experimental data with Eq. (11) provides a value of $\mu_e\tau_e = 9.3 \times 10^{-4}$ cm^2/V, which agrees well the longer lifetime component $\mu_e\tau_{e2} = 8.0 \times 10^{-4}$ cm^2/V obtained from the TOF measurement results shown in Fig. 17A and B. For hole transport, $\mu_h\tau_h$ is $\sim 3.2 \times 10^{-4}$ cm^2/V measured by TOF and $\sim 7.3 \times 10^{-4}$ cm^2/V deduced from the photocurrent-voltage characteristic shown in Fig. 17C. Moreover, knowing values for μ and τ separately for both types of carriers (electrons and holes) also allow the determination of the surface recombination velocities (S) of both electrons and holes from the photocurrent-voltage characteristics of the same sample. Fitting the photocurrent-voltage characteristics with Eq. (11) yields S/μ of about 420 V/cm for electrons, which provides S_e of about 1.4×10^4 cm/s for electrons. For holes, the fitted value of S/μ was about 76 V/cm, which yields a value of S_h of about 2.7×10^3 cm/s. The measured surface recombination velocities in h-^{10}BN are lower than those in typical GaN epilayers with $S_e \sim 5 \times 10^4$ cm/s (Aleksiejūnas et al., 2003) and $S_h \sim 1.7 \times 10^4$ cm/s (Shakya et al., 2004).

Fig. 16 Top panels: Schematics of a lateral photoconductive h-^{10}BN detector structure with Ni/Au metal bilayer contacts deposited on two edges for TOF measurements. The distance between the two electrodes is 2 mm. Bottom panels: Recorded temporal responses of output voltage after pulsed excitation by an excimer laser for (A) electron and (B) hole transport under a bias voltage of 90 V. The insets are the plots of the transit times as functions of applied electric field for photogenerated (A) electrons and (B) holes. *Reproduced from Maity, A., Grenadier, S.J., Li, J., Lin, J.Y., Jiang, H.X., 2018. Hexagonal boron nitride neutron detectors with high detection efficiencies. J. Appl. Phys. 123, 044501; Copyright (2018) AIP Publishing; Grenadier, S.J., Maity, A., Li, J., Lin, J.Y., Jiang, H.X., 2019. Lateral charge carrier transport properties of B-10 enriched hexagonal BN thick epilayers. Appl. Phys. Lett. 115, 072108; Copyright (2019) AIP Publishing.*

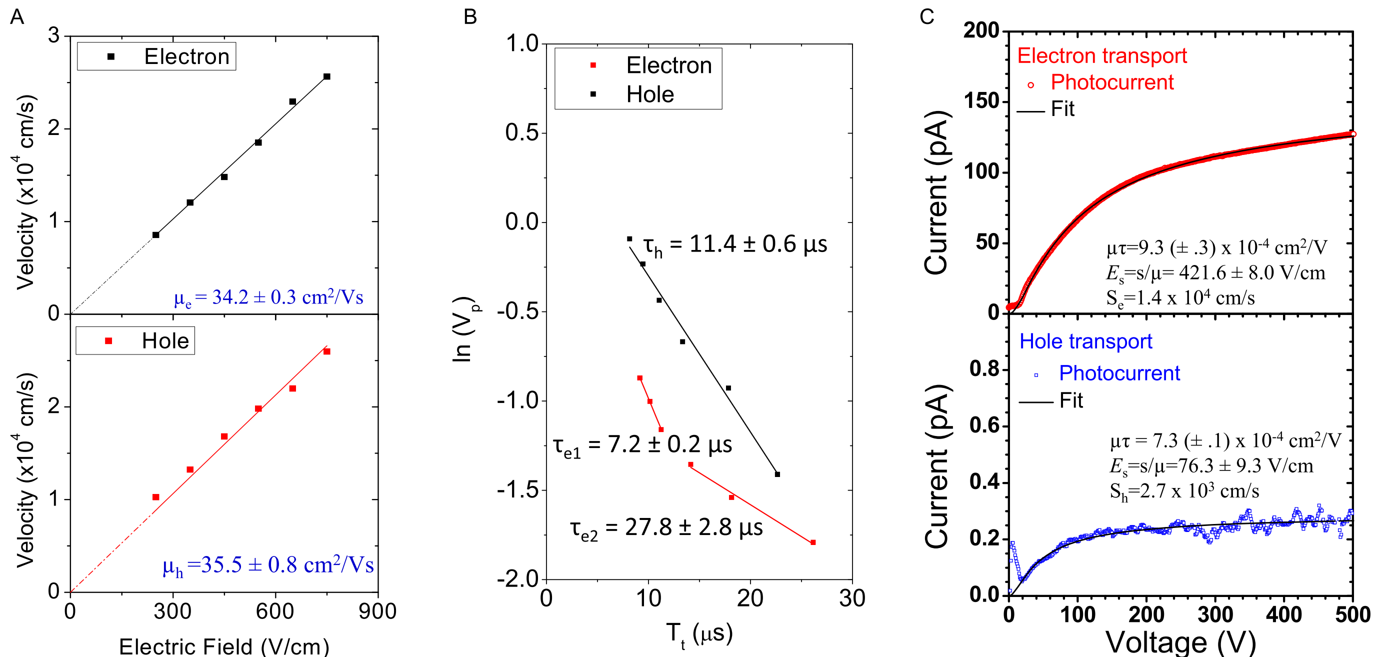

Fig. 17 (A) Carrier drift velocity vs applied electric field for electrons (Top panel) and holes (Bottom panel). The slope of the linear fit of the data provides the carrier drift mobility of h-^{10}BN in the lateral direction. (B) ln (V_p) (peak voltage) vs T_t (transit time) for electrons and holes. The linear fit of the data provides the trapping lifetime of drifted photo-generated carriers in h-BN. (C) Photocurrent-voltage characteristics for electron transport (Top panel) and hole transport (Bottom panel). The solid curves are fits with Eq. (11) and the fitted values of $\mu\tau$ product and S/μ as well as the deduced value of S are indicated inside the figures. *Reproduced from Grenadier, S.J., Maity, A., Li, J., Lin, J.Y., Jiang, H.X., 2019. Lateral charge carrier transport properties of B-10 enriched hexagonal BN thick epilayers. Appl. Phys. Lett. 115, 072108; Copyright (2019) AIP Publishing.*

It is worth mentioning that the measured $\mu\tau$ products in the lateral direction in h-^{10}BN for both electron and holes shown in Fig. 17 are about two orders of magnitude larger than those measured in the vertical direction (Maity et al., 2016, 2017a, 2018) such as that shown in Fig. 12. This is expected because like graphite (Gallos et al., 1994), h-BN is a layer structured material, in which very different bonding, i.e., strong covalent bonding within the basal planes and weak bonding between planes, which is expected to lead to anisotropy in electronic transport properties. The results are also consistent with a previous study which indicated that the mobility-lifetime products ($\mu\tau$) for both electrons and holes are larger in the lateral direction (within the basal planes) than in the vertical direction (between planes) (Dahal et al., 2016). Moreover, the measured surface recombination field (E_s) in the lateral detector shown in Fig. 17 is also nearly two orders of magnitude smaller than those in the vertical detectors (Maity et al., 2016, 2017a, 2018), such as that shown in Fig. 12A.

5.2 Attainment of 1 cm^2 h-^{10}BN lateral neutron detectors with unprecedented efficiency

As demonstrated through the $\mu\tau$ product measurement results, the lateral device architecture shown in Fig. 11B which utilizes the lateral transport properties is preferred over that of the vertical detector shown in Fig. 11A. Compared to the vertical detector scheme shown in Fig. 11A, the advantageous features of lateral detectors shown in Fig. 11B include: (1) higher lateral carrier mobilities and hence larger $\mu\tau$ products; (2) the effects of surface recombination, which have been identified as one of the major factors that limits the charge collection efficiency in h-BN vertical detectors (Maity et al., 2019b), are minimized in lateral detectors as shown in Fig. 11B because the contact area between the electrodes and the detector's surface is minimized; (3) comparing the device geometries between the vertical and lateral detectors shown in Fig. 11, for the same detection area and detector thickness, the device capacitance for the lateral detector is reduced by more than two orders of magnitude compared to that of the vertical detector, which makes scaling up the detection area more feasible.

More recently, the advantages of lateral device geometry have enabled the successful demonstration of neutron detectors with a detection area of 1 cm^2 with an unprecedently high detection efficiency at 59% (Maity et al., 2020). This 1 cm^2 h-^{10}BN detector was constructed from five h-^{10}BN lateral detector strips with an average strip width of $W = 1.2$ mm with the two electrodes deposited on the clipped edges of the h-^{10}BN strips,

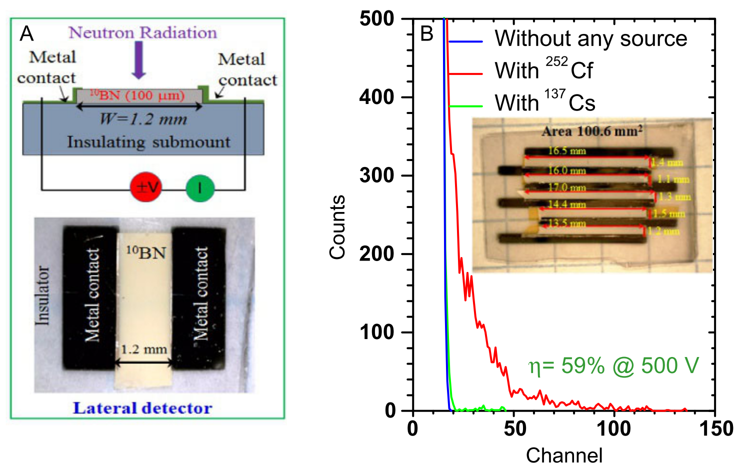

Fig. 18 (A) Schematic and optical image of a h-^{10}BN lateral detector strip. (B) The nuclear reaction pulse height spectra of a 1 cm^2 h-^{10}BN detector (red curves) in response to thermal neutrons from a moderated ^{252}Cf source at a bias voltage of $V_b = 500$ V. The blue curve is the background (or dark) counts measured at the same bias voltage. The green curve is the response to gamma photons produced by a ^{137}Cs gamma source measured at the same bias voltage. The inset is an optical image of this 1 cm^2 detector constructed from five h-^{10}BN lateral detector strips with an average strip width of $W = 1.2$ mm. *Reproduced from Maity, A., Grenadier, S.J., Li, J., Lin, J.Y., Jiang, H.X., 2020. High efficiency hexagonal boron nitride neutron detectors with 1 cm^2 detection areas. Appl. Phys. Lett. 116, 142102; Copyright (2020) AIP Publishing.*

as illustrated in Fig. 18A. Fig. 18B shows the pulse height spectra of this 1 cm^2 h-^{10}BN detector (Maity et al., 2020). The dark spectrum (blue) was recorded in the absence of any radiation source at 500 V, while the spectrum under thermal neutron irradiation (red) was measured at the same bias voltage. The green curve is the response to gamma photons emitted from a ^{137}Cs source under 10 mR/h exposure measured at the same bias voltage, which again shows that the h-^{10}BN detector has a negligible response to gamma photons. The pulse height spectrum under thermal neutron radiation was integrated beyond the highest dark channel (low level discriminator) to obtain the total number of counts. By comparing the total number of counts detected by the h-^{10}BN detector to that of a commercial ^{6}LiF filled micro-structured semiconductor neutron detector (MSND Domino™ V4) with an area of 4 cm^2 and a certified detection efficiency of 30 (±1)%, the detection efficiency (η) of the 1 cm^2 h-^{10}BN detector was determined to be 58.9 (±2.4)% at a bias voltage of 500 V, which represents the highest detection efficiency reported among all solid-state neutron detectors.

Realizing 1 cm^2 detectors with high detection efficiencies is a very critical first step for the eventual commercial adoption of h-BN detectors. Practical uses of solid-state neutron detectors often require detector arrays to provide adequate sensitivities. However, the minimum required size of individual detectors within an array is typically 1 cm^2. For example, the ^{6}LiF filled 4 cm^2 micro-structured Si semiconductor neutron detector (MSND Domino™ V4) commercially purchased from Radiation Detection Technologies, Inc. and used for the h-^{10}BN detector efficiency calibration is constructed from a combination of four 1 cm^2 detectors with a certified detection efficiency of about 30%.

The I-V characteristics of this 1 cm^2 h-^{10}BN detector incorporating five detector strips with an average strip width of 1.2 mm have been characterized in the dark (Fig. 19A) and under UV illumination (Fig. 19B) to extract the dark resistivity and the $\mu\tau$ products. Based on the measured dark resistance and the device geometry, the dark resistivity of the h-^{10}BN epilayer used to construct this 1 cm^2 detector is $\rho = 1 \times 10^{12}\,\Omega\cdot$cm. The dark resistivity value is about one order of magnitude larger than the minimum requirement of $2 \times 10^{11}\,\Omega\cdot$cm deduced by Eq. (7), which makes the high detection efficiency of this detector possible. Fitting the photocurrent-voltage characteristic under UV photon illumination in Fig. 19B by Eq. (11) yields values of $\mu_e\tau_e$ and s_e/μ_e for this detector of 5.0×10^{-3} cm^2/V and 5.5×10^2 V/cm, respectively, which provide values of $\frac{W^2}{V\mu_e\tau_e} \approx 0.007$ and $\frac{s_e/\mu_e}{V/W} \approx 0.14$ at a bias voltage of 500 V, and an expected charge collection efficiency of 87.4% under UV irradiation.

Based on the measured values of s_e/μ_e $(= E_s) = 5.5 \times 10^2$ V/cm and the electron mobility in the lateral direction in h-^{10}BN of $\mu_e \sim 35$ cm^2/V·s shown in Fig. 17A (Grenadier et al., 2019), the surface recombination velocity for electrons in h-^{10}BN can be deduced to be $s_e = 5.5 \times 10^2 \times 35 = 1.9 \times 10^4$ cm/s, which agrees reasonably well with a value of 1.4×10^4 cm/s measured by the TOF technique shown in Fig. 17C (Grenadier et al., 2019). It is important to recognize that the measured $\mu_e\tau_e$ product of 5.5×10^2 V/cm for this 1 cm^2 lateral detector is almost two orders of magnitude larger than those measured in the vertical detectors (Maity et al., 2016, 2017a, 2018) such as that shown in Fig. 12. Moreover, the $\mu_e\tau_e$ product of this 1 cm^2 lateral detector has also been improved over that in earlier lateral detectors (Grenadier et al., 2019; Maity et al., 2019a) such as that shown in Fig. 17. The improvements were achieved primarily through MOCVD epitaxial growth optimization, which ultimately made it possible to scale up the h-^{10}BN detector size to 1 cm^2 while retaining a high detection efficiency of 59% (Maity et al., 2020).

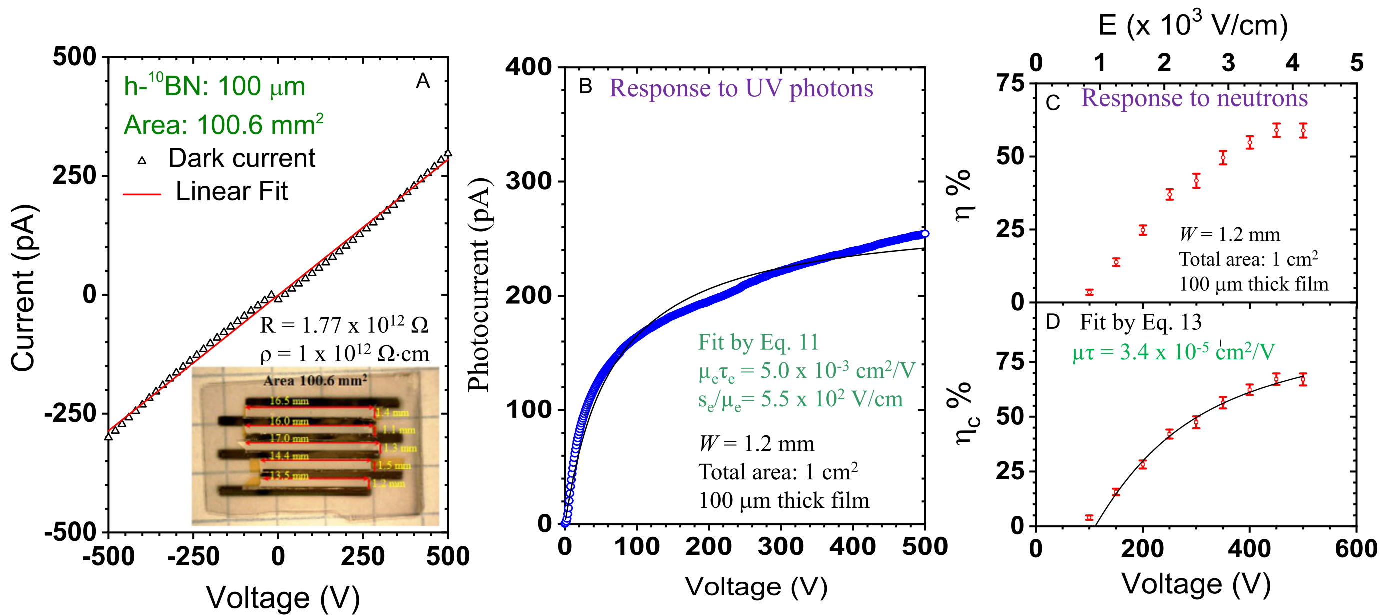

Fig. 19 I-V characteristics of the 1 cm^2 h-^{10}BN detector incorporating five detector strips with a film thickness of 100 μm and an average strip width of 1.2 mm under (A) dark and (B) UV photon illumination. (C) (Top panel) Measured thermal neutron detection efficiency (η) of the same detector as a function of the applied bias voltage. (Bottom panel) Charge collection efficiency (η_c) of the same detector as a function of the applied bias voltage, V, where η_c was calculated by dividing the measured detection efficiency by the expected theoretical efficiency of 100 μm thick ^{10}BN detector of 88%.

5.3 Characterizing transport parameters under thermal neutron irradiation

The 1 cm^2 detector of Fig. 18B was constructed by combining five narrow detector strips with an average strip width of W = 1.2 mm. The reason for using narrow detector strips is that the primary condition for achieving a high charge collection efficiency is as stated in Eq. (9). The condition of Eq. (9) means that the charge carrier drift length ($=\mu\tau E$) under neutron irradiation needs to be much larger than the carrier transit distance (W) to avoid bulk trapping, by considering the fact that on average the radiation-generated free charge carriers travel a distance of W prior to their extraction by the electrodes, where W is also the detector strip width. Based on Eq. (9), the detector strip width W, is limited by the value of the mobility-lifetime product ($\mu\tau$) of the detector material at a fixed bias voltage. However, this $\mu\tau$ product must be measured at the corresponding conditions under thermal neutron irradiation.

Compared to the vertical detectors, the metal contact area and the surface recombination field are significantly reduced. Moreover, the mobilities of electrons and holes in the lateral direction in h-BN are comparable (Cao et al., 2013; Grenadier et al., 2019; Semenoff, 1984), one can describe the I-V characteristics under radiation by a modified Many's equation for lateral transport by neglecting the effect of surface recombination,

$$I(V) = I_0\eta_c = 2I_0\left[\frac{V\mu\tau}{W^2} - \left(\frac{V\mu\tau}{W^2}\right)^2\left(1 - \exp\left(-\frac{w^2}{V\mu\tau}\right)\right)\right]. \tag{13}$$

The measured thermal neutron detection efficiency (η) and the charge collection efficiency (η_c) of the same 1 cm^2 lateral detector as functions of the applied bias voltage (V) are shown in Fig. 19C and D, respectively, where η_c was calculated by dividing the measured detection efficiency by the expected theoretical efficiency of 100 μm thick detector of 88%, based on Eq. (1) and Fig. 9B. Fitting η_c vs V under neutron irradiation with Eq. (13) provides a charge carrier $\mu\tau$ product of $\sim 3.4\times10^{-5}$ cm^2/V. Fitting the experimental data of the photocurrent-voltage characteristic under UV photon illumination in Fig. 19B with Eq. (13) again yields a carrier $\mu\tau$ product of 5×10^{-3} cm^2/V, which is in a reasonable agreement with the results obtained by fitting the measured data with Eq. (11). Since the measured $\mu\tau$ product under neutron irradiation of 3.4×10^{-5} cm^2/V and the detector strip width must satisfy the condition of Eq. (9), $W^2 < V\mu\tau$, in order to provide a high charge collection efficiency, this imposes a

limitation on the strip width at a given applied bias voltage. For this reason, we had to combine five narrow strips with W ~1.2 mm in order to provide the necessary condition for a high charge collection efficiency and hence a high overall detection efficiency.

For a given strip width, enhancing the $\mu\tau$ product would increase the detection efficiency or lower the required bias voltage. On the other hand, at a fixed bias voltage, enhancing the $\mu\tau$ product would relax the constrain in the detector strip width. Consider the 1 cm^2 detector as shown in Figs. 18 and 19, if we can increase the $\mu\tau$ product under neutron irradiation from 3×10^{-5} cm^2/V to 3×10^{-4} cm^2/V, the same detector of Fig. 18 will only require 50 V bias to achieve a detection efficiency of 60%. Moving a step further, if the $\mu\tau$ product under neutron irradiation is increased from 3×10^{-5} cm^2/V to 2×10^{-3} cm^2/V, under the same 500 V bias, we can increase the width of the detector strips (*W*) to 1.0 cm. This means that we only need one detector strip to form a 1 cm^2 detector, which will significantly reduce the fabrication steps and increase the device yield.

For the 1 cm^2 lateral detector shown in Figs. 18 and 19, the charge carrier $\mu\tau$ product obtained under thermal neutron irradiation of $\sim 3.4 \times 10^{-5}$ cm^2/V is more than two orders of magnitude lower than the value measured under UV illumination of $\sim 5 \times 10^{-3}$ cm^2/V. This is because UV illumination generates a higher charge carrier density than that generated by neutron irradiation. The presence of higher charge carrier density allows more traps to be filled by the charge carriers. The results thus indicate that the h-^{10}BN epilayer used to fabricate the 1 cm^2 detector contains charge traps, even though this detector delivered an unprecedentedly high detection efficiency among solid-state detectors as of today. The density of charge traps must be further reduced through growth process optimization in order to increase $\mu\tau$ product and to reduce the bias voltage required for the same strip width (*W*) or to increase *W* for a fixed bias voltage.

6. Dominant native and point defects in h-BN

6.1 Oxygen impurities

For the growth of thick h-^{10}BN epilayers, high growth temperatures and long growth times together with the use of sapphire substrates unavoidably introduce oxygen impurities into *h*-BN films due to oxygen diffusion from sapphire substrates. The results shown in Fig. 12 conclusively demonstrated that oxygen impurities are one of the major bulk defects in h-BN films (Grenadier et al., 2018). These oxygen impurities tend to act as substitutional

donors (O_N) (Weston et al., 2018). One of the most dramatic effects of O_N donor incorporation during high temperature growth shown in Fig. 12 is that the majority carrier type in h-BN epilayers changed from holes to electrons. As illustrated in Fig. 12, for epilayers grown at high temperatures such as 1500 °C, the $\mu\tau$ products of electrons are larger than those of holes. This is reversed for epilayers grown at lower temperature such as at or below 1400 °C (Doan et al., 2014b; Grenadier et al., 2018).

Fig. 20 compares the room temperature PL emission spectra of two *h*-BN epilayers, with one grown at a temperature of about 1400 °C and another at about 1500 °C (Grenadier et al., 2018). The sample grown at 1400 °C consists of a dominant broad transition peak at about 3.9 eV. This 3.9 eV line was believed to have the same physical origin as the previously observed donor-acceptor pair (DAP) transition peak superimposed within its phonon replicas covering from 3.7–4.1 eV, resulting from the recombination between V_N (nitrogen vacancy) donors and C_N (carbon impurity occupying nitrogen site) deep acceptors (Du et al., 2015). However, a new transition peak near 3.4 eV is clearly visible in the sample grown at a high temperature of 1500 °C. This transition peak also has a very board linewidth similar to the transition peak near 3.9 eV, which suggested

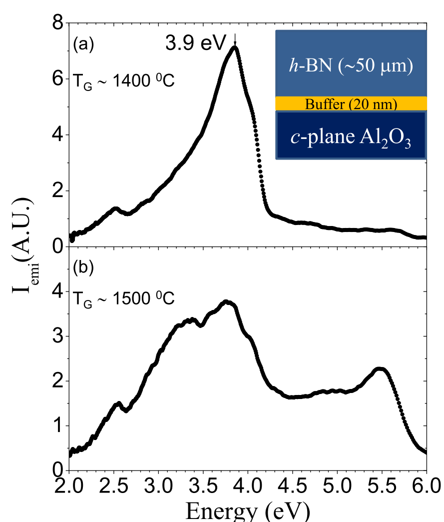

Fig. 20 Room temperature PL spectra of *h*-BN epilayers deposited on sapphire by MOCVD at different growth temperatures (A) $T_G \sim 1400$ °C and (B) $T_G \sim 1500$ °C. The inset shows a schematic of the *h*-BN epilayer structure. *Reproduced from Grenadier, S.J., Maity, A., Li, J., Lin, J.Y., Jiang, H.X., 2018. Origin and roles of oxygen impurities in hexagonal boron nitride epilayers. Appl. Phys. Lett. 112, 162103; Copyright (2018) AIP Publishing.*

that this new 3.4 eV emission can also be attributed to a DAP transition with the involved donor being O_N (Grenadier et al., 2018). From the energy difference between 3.9 eV and 3.4 eV and the assumed involved acceptor being the same C_N, the O_N donor involved in the 3.4 eV transition is expected to be about 0.5 eV deeper than the shallow donor of V_N. Since the measured energy level of V_N is about 0.1 eV (Du et al., 2015), the PL results shown in Fig. 20 therefore implied that the energy level of O_N in h-BN is about 0.6 eV.

Due to the highly resistive nature of these h-BN epilayers ($\rho > 10^{14}\,\Omega\cdot$cm), probing the temperature dependence of the carrier concentration using Hall effect measurements was challenging. In order to further characterize the energy level of O_N donors, the *h*-BN epilayer grown under 1500 °C was diced into pieces with a lateral dimension of 1 mm × 1 mm and a Ni/Au (10 nm/20 nm) bilayer was deposited on both sides of the 1 mm × 1 mm free-standing samples using e-beam evaporation, as schematically shown in the inset of Fig. 21A to form vertical photoconductive detectors (Grenadier et al., 2018). Dark current characteristics were measured at different temperatures to deduce the temperature dependent resistivity of the sample. A room temperature current density vs voltage (J-V) curve is plotted in Fig. 21A. The dark resistances (R) of this sample measured at different temperatures are shown in Fig. 21B. The Arrhenius plot of the measured resistance provided an activation energy for O_N donors of about 0.56 eV, which is in reasonable agreement with the value deduced from the PL results shown in Fig. 20.

6.2 Probing dominant defects by photoexcitation spectroscopy

Accompanying the incorporation of O_N donor impurities is the decrease in the formation energies and hence generation of other deep level acceptors such as boron vacancy—hydrogen complexes (V_B-H) (Weston et al., 2018). This together with the fact that the growth rate of thick h-^{10}BN epilayers is many times higher than the typical growth rate of ~1 μm/h employed for III-nitride epilayers grown by MOCVD makes possible the formation of boron vacancies and their complexes. Previous theoretical and experimental studies have also suggested that nitrogen vacancies (V_N) and carbon impurities occupying the nitrogen sites (C_N) in *h*-BN are relatively easy to incorporate during the crystal growth of *h*-BN (Attaccalite et al., 2011; Fanciulli and Moustakas, 1993; Huang and Lee, 2012; Jimenez et al., 1997; Ngwenya et al., 2011; Orellana and Chacham, 2001; Silly et al., 2007; Vokhmintsev and Weinstein, 2021; Vokhmintsev et al., 2019; Wang et al., 2012; Zunger

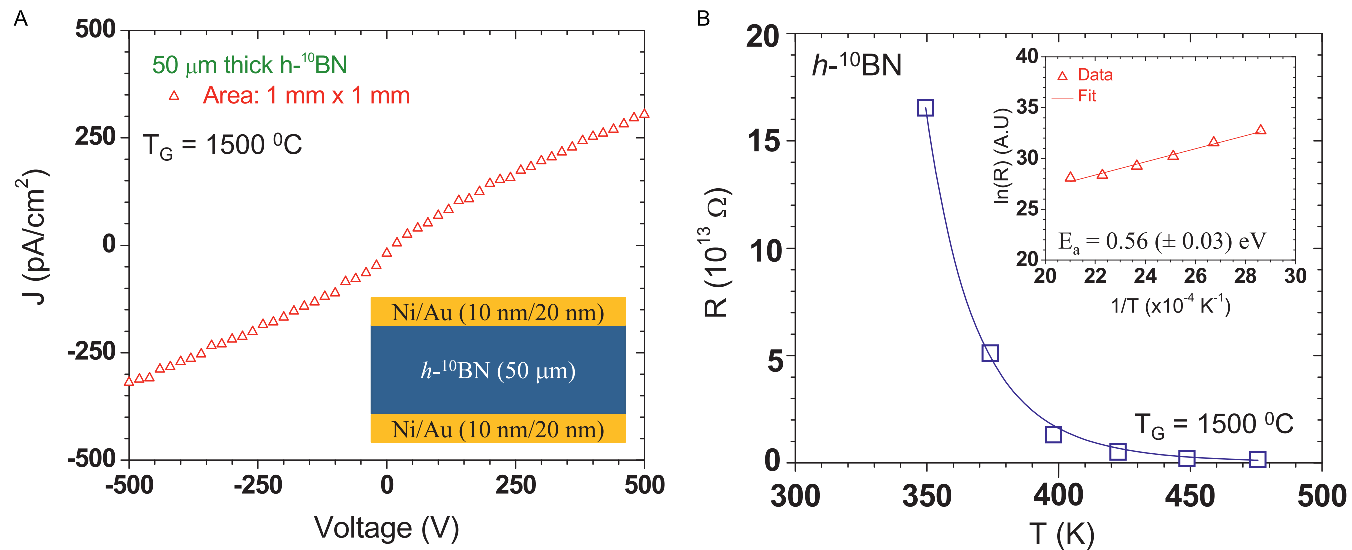

Fig. 21 (A) Room temperature dark current density vs voltage (J-V) characteristic of a 50 μm thick freestanding h-BN sample grown at 1500 °C. The inset shows a schematic of the freestanding h-BN sample with Ni/Au (10 nm/20 nm) ohmic contacts deposited on both top and bottom surfaces for electrical characterization. (B) The temperature dependence of the dark resistance of the same freestanding h-BN sample measured in the vertical direction (along the c-axis). The inset shows the Arrhenius plot of the measured resistance, providing an activation energy of about 0.56 eV for O_N donors. *Reproduced from Grenadier, S.J., Maity, A., Li, J., Lin, J.Y., Jiang, H.X., 2018. Origin and roles of oxygen impurities in hexagonal boron nitride epilayers. Appl. Phys. Lett. 112, 162103; Copyright (2018) AIP Publishing.*

and Katzir, 1975), pointing to the importance of minimizing the density of nitrogen vacancies (V_N) (Du et al., 2015, 2016). Among the impurities and defects in *h*-BN, C_N is also believed to be the most probable acceptor (Attaccalite et al., 2011; Huang and Lee, 2012; Ngwenya et al., 2011). Its calculated energy level is around 1.1 eV and 3.2 eV obtained by LDA and G_0W_0 methods, respectively (Huang and Lee, 2012). Previous theoretical studies have also indicated that a substitutional carbon impurity on a nitrogen site could induce two deep defect levels localized on the carbon atom (Attaccalite et al., 2011; Huang and Lee, 2012). The experimentally measured energy levels of C_N acceptors range from 1.2 eV to ~2.3 eV (Attaccalite et al., 2011; Du et al., 2015, 2016; Vokhmintsev et al., 2019; Wang et al., 2012). The calculated acceptor energy levels involving (V_B-H) and (V_B-2H) complexes are 1.65 and 1.54 eV, respectively. Scattering with these defects will reduce the carrier $\mu\tau$ products in h-BN.

A lateral geometry device was fabricated from a 98 μm thick freestanding h-^{10}BN epilayer to probe the effects of defects on the electron and hole transport. The measured dark resistivity of the sample was $1.25 \times 10^{13}\,\Omega\cdot$cm. The schematic of the fabricated lateral photoconductive type devices (with an exposed area of 2 mm × 4 mm) is shown in Fig. 22A. A light source covering the wavelength range of 170–2100 nm [EQ-99 by Energytiq] coupled with a triple grating monochromator (Acton SP2300i) was used as a variable wavelength excitation source with a spectral resolution of ~0.2 nm to perform the photocurrent spectroscopy measurements. A 300 μm × 4 mm metal slit was used to allow light to enter and illuminate only near one of the metal contacts. If the electrode near the illuminated area is positively (negatively) biased, holes (electrons) travel a much longer distance compared to electrons (holes) before being extracted at the electrodes. This scheme enables us to probe the photocurrent for holes and electrons separately, as schematically illustrated in Fig. 22A.

The photocurrent excitation spectrum for hole conduction measured at $V = 1000$ V is shown in the top panel of Fig. 22B. The spectrum has been normalized to the emission spectrum of the UV light source and is featureless between 3.0 and 5.8 eV. The most prominent feature is a steep decrease in the photocurrent of hole conduction at a photon energy of about 5.9 eV. The photocurrent excitation spectrum for electron conduction measured at $V = 400$ V is shown in the bottom panel of Fig. 22B, in which the most notable feature exhibited is a sharp increase in the photocurrent at a photon energy of about 4.9 eV.

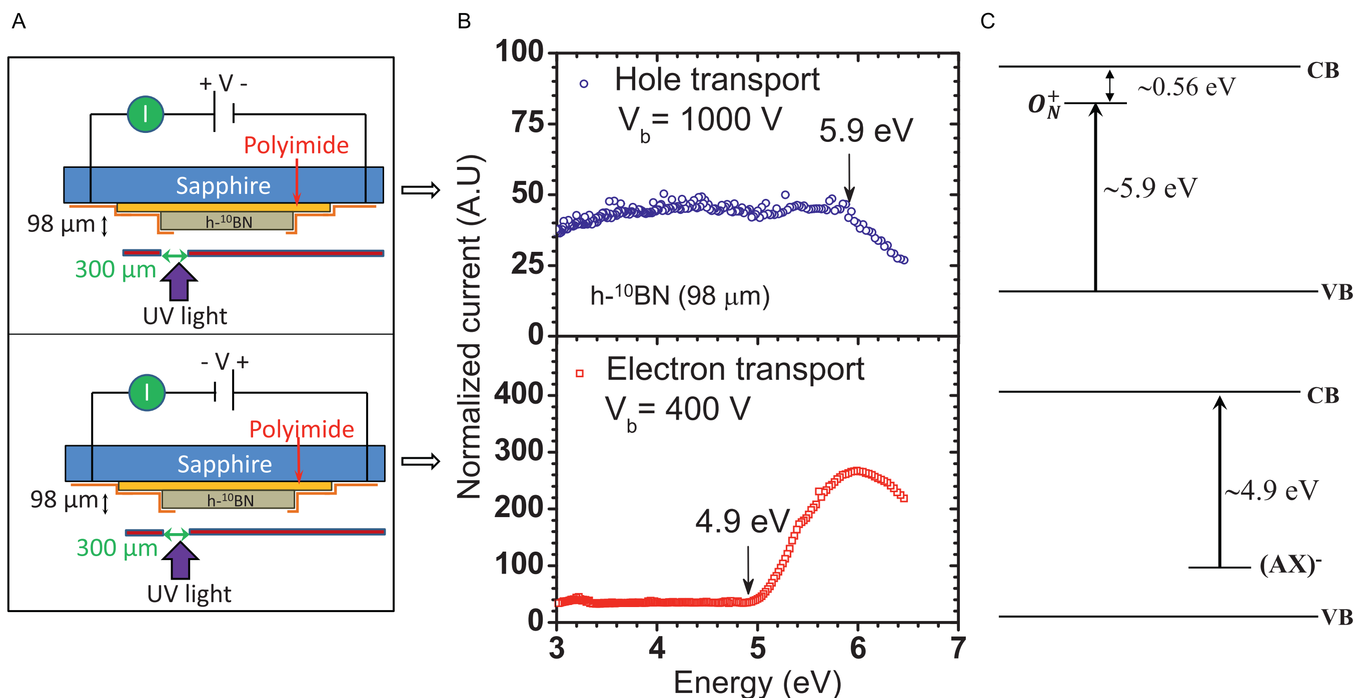

Fig. 22 (A) Schematic diagrams and (B) measured photocurrent excitation spectra for hole (top panel) and electron (bottom panel) transport, measured at bias voltages of 1000 and 400 V, respectively. A threshold photon energy for a sharp decrease in photocurrent is observed at ~5.9 eV for hole conduction, whereas a threshold photon energy for a sharp increase in photocurrent is observed at ~4.9 eV for electron conduction. (C) (Top panel): Energy band diagram illustrating photoexcitation of electrons from the valence band to O_N^+ donors with a threshold photon energy of ~5.9 eV; (Bottom panel): Photoexcitation of electrons from acceptors/acceptor complexes to the conduction band with a threshold photon energy of ~4.9 eV.

During h-^{10}BN wafer growth at high temperatures, the formation processes of impurities and defects likely involve the following steps: (a) Diffusion of oxygen impurities from the sapphire substrate which replace N atoms to form O_N, (b) the Fermi level, E_f, moving toward the conduction band edge due to an increased O_N concentration, and (c) the subsequent formation of compensating acceptors due to decreasing formation energy (E_{form}) as E_f moving toward to the conduction band edge (Weston et al., 2018). In such a scenario, O_N donors are primary impurities, whereas the acceptors or acceptor complexes (AX) are the secondary compensating impurities. As a result, the concentration of O_N impurities is higher than that of (AX) in thick *h*-BN epilayers grown at high temperatures. As such, the dark current is primarily contributed by the background electron concentration (n_0) associated with the activation of the net of [O_N-(AX)]. Photocurrents effectively record variations in the free carrier concentration (electrons or holes). As such, the threshold photon energies in the photocurrent excitation spectra represent the minimum energies required to generate free carriers from different energy levels (impurities or bands). Therefore, the changes in photocurrents observed in Fig. 22B are due to changes in the background electron concentration because of free carrier excitation from different energy levels.

The photoexcitation spectrum of hole transport shown in the top panel of Fig. 22B can be described by the excitation process illustrated in the top panel of Fig. 22C, $O_N^+ + h\nu\ (5.9\ eV) \rightarrow O_N^0 + h^+$, which generates free holes, Δp, in the valence band. The photogenerated net holes (Δp) will recombine with a fraction of the background electrons. As a result, the free electron concentration in the conduction band is decreased from n_0 to n_0-Δp upon photoexcitation by photons with an energy $h\nu \geq 5.9$ eV, which manifested itself as a decrease in the photocurrent at a threshold photon energy of about 5.9 eV, as seen in the top panel of Fig. 22B.

On the other hand, the photoexcitation spectrum of electron transport shown in the bottom panel of Fig. 22B can be described by the photoexcitation process illustrated in the bottom panel of Fig. 22C, $(AX)^- + h\nu\ (4.9\ eV) \rightarrow (AX)^0 + e^-$. Under photoexcitation by photons with $h\nu \geq 4.9$ eV, the free electron concentration in the conduction band is increased from n_0 to $n_0 + \Delta n$, which results in an increase in the photocurrent at a threshold photon energy of 4.9 eV, as observed in the bottom panel of Fig. 22B. Possible origins of the dominant deep acceptors and acceptor complexes are C_N, V_B-H and V_B-2H (Attaccalite et al., 2011; Huang and Lee, 2012; Ngwenya et al., 2011; Weston et al., 2018). Significant improvements

in material quality and electrical transport parameters of h-BN epilayers are anticipated by further optimizing the MOCVD growth processes to minimize the identified dominant defects, including V_N, O_N, C_N, V_B-H and V_B-2H.

7. Concluding remarks

Significant progresses in MOCVD epitaxial growth, understanding of the electrical transport properties and device applications of h-BN have been attained over the last 10 years. In particular, B-10 enriched freestanding h-BN epilayers with large thicknesses up to 200 μm have been realized as of this writing. The high temperature mobility (μ) and room temperature mobility-lifetime (μτ) product characterization results suggested that typical unintentionally doped h-BN epilayers grown at a temperature at or below 1400 °C tend to exhibit a weak p-type conductivity, possibly due to the presence of acceptor-like deep level native defects. Intentional doping studies have revealed that Si and C dopants introduce relatively deep donor levels at 1.2 and 0.45 eV, respectively, whereas Mg doping has yielded h-BN epilayers with a p-type conductivity as low as 2 Ω·cm. Practical p-n junction devices based on h-BN epilayers have yet to be demonstrated.

Photoconductive-type detectors fabricated from freestanding h-^{10}BN epilayers have shown great promises for thermal neutron detector applications. These detectors exhibit very high electrical resistivities and extremely low dark currents due to the ultrawide bandgap of h-BN. Compared to typical vertical detectors, it was shown that the lateral photoconductive-type detectors possess enhanced μτ products due to the layered structure of h-BN and reduced surface recombination fields as well as reduced capacitance due to a reduction of the metal/semiconductor contact surface area. The advantageous features of the lateral device architecture have enabled the scale up of h-^{10}BN detector size to 1 cm^2 with a detection efficiency of 59% for thermal neutrons. This detection efficiency represents the highest on record among all solid-state thermal neutron detectors to date.

It was noted that high growth temperatures, long growth times and the use of a sapphire substrate tend to incorporate oxygen related donor impurities into h-^{10}BN epilayers as a result of oxygen diffusion from the sapphire substrate. Consequently, the majority carrier type changes from holes in typical h-BN epilayers to electrons in epilayers grown at growth temperatures of $T_G > 1500$ °C. The energy level of O_N in h-BN has been determined to be about 0.56 eV from temperature dependent resistivity measurements.

Furthermore, accompanying the process of oxygen diffusion at high growth temperatures is the incorporation of compensating deep level acceptor-like point defects. Overall, these results suggested that future directions need to focus on further advancing the MOCVD growth processes for producing h-BN epilayers with reduced impurities including oxygen, carbon, and cation- and anion-vacancy related defect complexes to further enhance electrical resistivity and carrier mobility-lifetime $\mu\tau$ products.

Acknowledgments

The h-BN material and neutron detector research are supported by DOE ARPA-E (DE-AR0001257). The development of h-BN material and device technologies at TTU has been supported by DOE ARPA-E (DE-AR0000964) and (DE-AR0001257), NNSA SSAP program (DE-NA0002927) and (DE-FG02-09ER46552); DHS ARI Program (No. 2011-DN077-ARI048); NSF (DMR-1206652) and (ECCS-1402886); and DARPA-CMUVT program. H. X. Jiang and J. Y. Lin are grateful to the AT&T Foundation for the support of Ed Whitacre and Linda Whitacre endowed chairs.

References

Ahmed, K., Dahal, R., Weltz, A., Lu, J.J.Q., Danon, Y., Bhat, I.B., 2017. Solid-state neutron detectors based on thickness scalable hexagonal boron nitride. Appl. Phys. Lett. 110, 023503.

Aleksiejūnas, R., Sūdžius, M., Malinauskas, T., Vaitkus, J., Jarašiūnas, K., 2003. Determination of free carrier bipolar diffusion coefficient and surface recombination velocity of undoped GaN epilayers. Appl. Phys. Lett. 83, 1157.

Alem, N., Erni, R., Kisielowski, C., Rossell, M.D., Gannett, W., Zettl, A., 2009. Atomically thin hexagonal boron nitride probed by ultrahigh-resolution transmission electron microscopy. Phys. Rev. B 80, 155425.

Arnaud, B., Lebe'gue, S., Rabiller, P., Alouani, M., 2006. Huge excitonic effects in layered hexagonal boron nitride. Phys. Rev. Lett. 96, 026402.

Attaccalite, C., Bockstedte, M., Marini, A., Rubio, A., Wirtz, L., 2011. Coupling of excitons and defect states in boron-nitride nanostructures. Phys. Rev. B 83, 144115.

Bahandary, S., Sanyal, B., 2012. Graphene-Boron Nitride Composite: A Material With Advanced Functionalities. InTech.

Bellinger, S.L., Fronk, R.G., McGregor, D.S., 2014. Method of Fabricating a Neutron Detector such as a Microstructured Semiconductor Neutron Detector. US patent 8778715.

Bellinger, S.L., Fronk, R.G., McNeil, W.J., Sobering, T.J., McGregor, D.S., 2012a. Improved high efficiency stacked microstructured neutron detectors backfilled with nanoparticle 6LiF. IEEE Trans. Nucl. Sci. 59, 167.

Bellinger, S.L., Fronk, R.G., Sobering, T.J., McGregor, D.S., 2012b. High-efficiency microstructured semiconductor neutron detectors that are arrayed, dual-integrated, and stacked. Appl. Radiat. Isot. 70, 1121.

Britnell, L., Gorbachev, R.V., Jalil, R., Belle, B.D., Schedin, F., Mishchenko, A., Georgiou, T., Katsnelson, M.I., Eaves, L., Morozov, S.V., Peres, N.M.R., Leist, J., Geim, A.K., Novoselov, K.S., Ponomarenko, L.A., 2012. Field-effect tunneling transistor based on vertical graphene heterostructures. Science 335, 947.

Caldwell, J.D., Aharonovich, I., Cassabois, G., Edgar, J.H., Gil, B., Basov, D.N., 2019. Photonics with hexagonal boron nitride. Nat. Rev. Mater. 4, 552.
Cao, X.K., Clubine, B., Edgar, J.H., Lin, J.Y., Jiang, H.X., 2013. Two-dimensional excitons in three-dimensional hexagonal boron nitride. Appl. Phys. Lett. 103, 191106.
Chen, B., Lee, C.S., Lee, S.T., Webb, P., Chan, Y.C., Gambling, W., Tian, H., Zhu, W., 2000. Improved time-of-flight technique for measuring carrier mobility in thin films of organic electroluminescent materials. Jpn. J. Appl. Phys. 39 (3R), 1190.
Chopra, N.G., Luyken, R.J., Cherrey, K., Crespi, V.H., Cohen, M.L., Louie, S.G., Zettl, A., 1995. Boron-nitride nanotubes. Science 269, 966.
Chubarov, M., Pedersen, H., Högberg, H., Filippov, S., Engelbrecht, J.A.A., O'Connel, J., Henry, A., 2014. Boron nitride: a new photonic material. Physica B 439, 29.
Chugh, D., Wong-Leung, J., Li, L., Lysevych, M., Tan, H.H., Jagadish, C., 2018. Flow modulation epitaxy of hexagonal boron nitride. 2D Mater. 5, 045018.
Clinton, J., 2011. Optimization and Characterization of a Novel Shelf Powered Solid State Neutron Detector (Ph.D. thesis). Rensselaer Polytechnic Institute, New York, USA, pp. 73–78. Chap. 3.
Dahal, R., Huang, J.K., Lu, J.Q., Danon, Y., Bhat, I.B., 2015. Neutron-Detecting Apparatuses and Fabrication Methods. US patent 9151853B2.
Dahal, R., Li, J., Majety, S., Pantha, B.N., Cao, X.K., Lin, J.Y., Jiang, H.X., 2011. Epitaxially grown semiconducting hexagonal boron nitride as a deep ultraviolet photonic material. Appl. Phys. Lett. 98, 211110.
Dahal, R., Huang, K.C., Cliton, J., LiCausi, N., Lu, J.-Q., Danon, Y., Bhat, I., 2012. Self-powered micro-structured solid-state neutron detector with very low leakage current and high efficiency. Appl. Phys. Lett. 100, 243507.
Dahal, R., Ahmed, K., Woei Wu, J., Weltz, A., Lu, J., Danon, Y., Bhat, I.B., 2016. Anisotropic charge carrier transport in free-standing hexagonal boron nitride thin films. Appl. Phys. Express 9, 065801.
Dean, C.R., Young, A.F., Meric, I., Lee, C., Wang, L., Sorgenfrei, S., Watanabe, K., Taniguchi, T., Kim, P., Shepard, K.L., Hone, J., 2010. Boron nitride substrates for high-quality graphene electronics. Nat. Nanotechnol. 5, 722.
Dean, C., Young, A.F., Wang, L., Meric, I., Lee, G.-H., Watanabe, K., Taniguchi, T., Shepard, K., Kim, P., Hone, J., 2012. Graphene based heterostructures. Solid State Commun. 152, 1275.
Doan, T.C., Majety, S., Grendadier, S., Li, J., Lin, J.Y., Jiang, H.X., 2014a. Fabrication and characterization of solid-state thermal neutron detectors based on hexagonal boron nitride epilayers. Nucl. Instrum. Methods Phys. Res., Sect. A 748, 84.
Doan, T.C., Li, J., Lin, J.Y., Jiang, H.X., 2014b. Charge carrier transport properties in layer structured hexagonal boron nitride. AIP Adv. 4, 107126.
Doan, T.C., Li, J., Lin, J.Y., Jiang, H.X., 2016a. Growth and device processing of hexagonal boron nitride epilayers for thermal neutron and deep ultraviolet detectors. AIP Adv. 6, 075213.
Doan, T.C., Li, J., Lin, J.Y., Jiang, H.X., 2016b. Bandgap and exciton binding energies of hexagonal boron nitride probed by photocurrent excitation spectroscopy. Appl. Phys. Lett. 109, 122101.
Doty, F.P., 2004. Sandia National Laboratories, Boron Nitride Solid-State Neutron Detector. US patent, 6727504.
Du, X.Z., Li, J., Lin, J.Y., Jiang, H.X., 2015. The origin of deep-level impurity transitions in hexagonal boron nitride. Appl. Phys. Lett. 106, 021110.
Du, X.Z., Li, J., Lin, J.Y., Jiang, H.X., 2016. The origins of near band-edge transitions in hexagonal boron nitride epilayers. Appl. Phys. Lett. 108, 052106.
Fanciulli, M., Moustakas, T.D., 1993. Study of defects in wide band gap semiconductors by electron paramagnetic resonance. Physica B 185, 228.

Fujimoto, Y., Saito, S., 2016. Effects of strain on carbon donors and acceptors in hexagonal boron nitride monolayers. Phys. Rev. B 93, 045402.
Gallos, L.K., Anagnostopoulos, A.N., Argyrakis, P., 1994. Conduction anisotropy in layered semiconductors. Phys. Rev. B50, 14643.
Geim, A.K., Grigorieva, I.V., 2013. Van der Waals heterostructures. Nature 499, 419.
Gorczyca, I., Christensen, N.E., Svane, A., 2002. Influence of hydrostatic pressure on cation vacancies in GaN, AlN, and GaAs. Phys. Rev. B 66, 075210.
Grenadier, S.J., Maity, A., Li, J., Lin, J.Y., Jiang, H.X., 2018. Origin and roles of oxygen impurities in hexagonal boron nitride epilayers. Appl. Phys. Lett. 112, 162103.
Grenadier, S.J., Maity, A., Li, J., Lin, J.Y., Jiang, H.X., 2019. Lateral charge carrier transport properties of B-10 enriched hexagonal BN thick epilayers. Appl. Phys. Lett. 115, 072108.
Guan, Z.P., Li, J.Z., Zhang, G.Y., Jin, S.X., Ding, X.M., 2000. Minority electron mobility in a p-n GaN photodetector. Semicond. Sci. Technol. 15, 51.
Hao, G.D., Tsuzuki, S., Inoue, S.I., 2019. Small valence band offset of h-BN/$Al_{0.7}Ga_{0.3}N$ heterojunction measured by X-ray photoelectron spectroscopy. Appl. Phys. Lett. 114, 011603.
He, B., Zhang, W.J., Yao, Z.Q., Chong, Y.M., Yang, Y., Ye, Q., Pan, X.J., Zapien, J.A., Bello, I., Lee, S.T., Gerhards, I., Zutz, H., Hofsass, H., 2009. P-type conduction in beryllium-implanted hexagonal boron nitride films. Appl. Phys. Lett. 95, 252106.
He, B., Qiu, M., Yuen, M.F., Zhang, W.J., 2014. Electrical properties and electronic structure of Si-implanted hexagonal boron nitride films. Appl. Phys. Lett. 105, 012104.
Henck, H., Pierucci, D., Fugallo, G., Avila, J., Cassabois, G., Dappe, Y.J., Silly, M.G., Chen, C., Gil, B., Gatti, M., Sottile, F., Sirotti, F., Asensio, M.C., Ouerghi, A., 2017. Direct observation of the band structure in bulk hexagonal boron nitride. Phys. Rev. B 95, 085410.
Huang, B., Lee, H., 2012. Defect and impurity properties of hexagonal boron nitride: a first-principles calculation. Phys. Rev. B 86, 245406.
Huang, B., Cao, X.K., Jiang, H.X., Lin, J.Y., Wei, S.H., 2012. Origin of the significantly enhanced optical transitions in layered boron nitride. Phys. Rev. B 86, 155202.
Isberg, J., Hammersberg, J., Johansson, E., Wikström, T., Twitchen, D.J., Whitehead, A.J., Coe, S.E., Scarsbrook, G.A., 2002. High carrier mobility in single-crystal plasma-deposited diamond. Science 297, 1670.
Jiang, H.X., Lin, J.Y., 2014. Hexagonal boron nitride for deep ultraviolet photonic devices. Semicond. Sci. Technol. 29, 084003.
Jiang, H.X., Lin, J.Y., 2017. Review—hexagonal boron nitride epilayers: growth, optical properties and device applications. ECS J. Solid State Sci. Technol. 6, Q3012.
Jiang, H.X., Majety, S., Dahal, R., Li, J., Lin, J.Y., 2015. Structures and Devices Based on Boron Nitride and Boron Nitride-III-Nitride Heterostructures. US patent 9,093,581. https://patents.justia.com/patent/9093581.
Jimenez, I., Jankowski, A.F., Terminello, L.J., Sutherland, D.G.J., Carlisle, J.A., Doll, G.L., Tong, W.M., Shuh, D.K., Himpsel, F.J., 1997. Core-level photoabsorption study of defects and metastable bonding configurations in boron nitride. Phys. Rev. B 55, 12025.
Klein, C.A., 1968. Bandgap dependence and related features of radiation ionization energies in semiconductors. J. Appl. Phys. 39, 2029.
Knoll, G.F., 1995. Radiation detection and measurement. In: Tsoulfanidis, N. (Ed.), Measurement and Detection of Radiation, third ed. Taylor & Francis, Washington, pp. 131–137. J. Wiley, 2000.
Kobayashi, Y., Akasaka, T., Makimoto, T., 2008. Hexagonal boron nitride grown by MOVPE. J. Cryst. Growth 310, 5048.
Kubota, Y., Watanabe, K., Tsuda, O., Taniguchi, T., 2007. Deep ultraviolet light-emitting hexagonal boron nitride synthesized at atmospheric pressure. Science 317, 932.

Laleyan, D.A., Zhao, S., Woo, S.Y., Tran, H.N., Le, H.B., Szkopek, T., Guo, H., Botton, G.A., Mi, Z., 2017. AlN/h-BN heterostructures for Mg dopant-free deep ultraviolet photonics. Nano Lett. 17, 3738.

Lebedev, E., Dittrich, T., Petrova-Koch, V., Karg, S., Brütting, W., 1997. Charge carrier mobility in poly(p-phenylenevinylene) studied by the time-of-flight technique. Appl. Phys. Lett. 71, 2686.

Li, J., Dahal, R., Majety, S., Lin, J.Y., Jiang, H.X., 2011. Hexagonal boron nitride epitaxial layers as neutron detector materials. Nucl. Instrum. Methods Phys. Res., Sect. A 654, 417.

Li, J., Majety, S., Dahal, R., Zhao, W.P., Lin, J.Y., Jiang, H.X., 2012. Dielectric strength, optical absorption, and deep ultraviolet detectors of hexagonal boron nitride epilayers. Appl. Phys. Lett. 101, 171112.

Li, X., Sundaram, S., El Gmili, Y., Ayari, T., Puybaret, R., Patriarche, G., Voss, P.L., Salvestrini, J.P., Ougazzaden, A., 2016. Large-area two-dimensional layered hexagonal boron nitride grown on sapphire by metalorganic vapor phase epitaxy. Cryst. Growth Des. 16, 3409.

Losovyj, Y.B., Ketsman, I., Sokolov, A., Belashchenko, K.D., Dowben, P., Tang, J., Wang, Z., 2007. The electronic structure change with Gd doping of HfO_2HfO_2 on silicon. Appl. Phys. Lett. 91, 132908.

Lu, M., Bousetta, A., Bensaoula, A., Waters, K., Schultz, J.A., 1996. Electrical properties of boron nitride thin films grown by neutralized nitrogen ion assisted vapor deposition. Appl. Phys. Lett. 68, 622.

Lynch, R.W., Drickamer, H.G., 1966. Effect of high pressure on the lattice parameters of diamond, graphite, and hexagonal boron nitride. J. Chem. Phys. 44, 181.

Lyons, J.L., Janotti, A., Van de Walle, C.G., 2014. Effects of carbon on the electrical and optical properties of InN, GaN, and AlN. Phys. Rev. B 89, 035204.

Madelung, O, Landolt-Bornstein (Eds.), 1987. Numerical data and functional relationships in science and technology. New Series. Group III: Crystal and Solid State Physics. Semiconductors. Subvolume a: Intrinsic Properties of Group IV Elements and III-V, II-VI and I-VII Compounds. vol. 22. Springer, Berlin, pp. XII–+ 451 pp.

Maity, A., Doan, T.C., Li, J., Lin, J.Y., Jiang, H.X., 2016. Realization of highly efficient hexagonal boron nitride neutron detectors. Appl. Phys. Lett. 109, 072101.

Maity, A., Grenadier, S.J., Li, J., Lin, J.Y., Jiang, H.X., 2017a. Toward achieving flexible and high sensitivity hexagonal boron nitride neutron detectors. Appl. Phys. Lett. 111, 033507.

Maity, A., Grenadier, S.J., Li, J., Lin, J.Y., Jiang, H.X., 2017b. High-efficiency and high-sensitivity thermal neutron detectors based on hexagonal BN epilayers. In: Proc. SPIE 10392, Hard X-Ray, Gamma-Ray, and Neutron Detector Physics XIX, 103920L.

Maity, A., Grenadier, S.J., Li, J., Lin, J.Y., Jiang, H.X., 2018. Hexagonal boron nitride neutron detectors with high detection efficiencies. J. Appl. Phys. 123, 044501.

Maity, A., Grenadier, S.J., Li, J., Lin, J.Y., Jiang, H.X., 2019a. High sensitivity hexagonal boron nitride lateral neutron detectors. Appl. Phys. Lett. 114, 222102.

Maity, A., Grenadier, S.J., Li, J., Lin, J.Y., Jiang, H.X., 2019b. Effects of surface recombination on the charge collection in h-BN neutron detectors. J. Appl. Phys. 125, 104501.

Maity, A., Grenadier, S.J., Li, J., Lin, J.Y., Jiang, H.X., 2020. High efficiency hexagonal boron nitride neutron detectors with 1 cm^2 detection areas. Appl. Phys. Lett. 116, 142102.

Majety, S., Li, J., Cao, X.K., Dahal, R., Pantha, B.N., Lin, J.Y., Jiang, H.X., 2012a. Epitaxial growth and demonstration of hexagonal BN/AlGaN p-n junctions for deep ultraviolet photonics. Appl. Phys. Lett. 100, 061121.

Majety, S., Cao, X.K., Li, J., Dahal, R., Lin, J.Y., Jiang, H.X., 2012b. Band-edge transitions in hexagonal boron nitride epilayers. Appl. Phys. Lett. 101, 051110.

Majety, S., Doan, T.C., Li, J., Lin, J.Y., Jiang, H.X., 2013a. Electrical transport properties of Si-doped hexagonal boron nitride epilayers. AIP Adv. 3, 122116.
Majety, S., Li, J., Zhao, W.P., Huang, B., Wei, S.H., Lin, J.Y., Jiang, H.X., 2013b. Hexagonal boron nitride and 6H-SiC heterostructures. Appl. Phys. Lett. 102, 213505.
Many, A., 1965. High-field effects in photoconducting cadmium sulphide. J. Phys. Chem. Solids 26, 575.
Mattila, T., Nieminen, R.M., 1997. Point-defect complexes and broadband luminescence in GaN and AlN. Phys. Rev. B 55, 9571.
McGregor, D.S., Unruh, T.C., McNeil, W.J., 2008. Thermal neutron detection with pyrolytic boron nitride. Nucl. Inst. Methods Phys. Res. A 591, 530.
Nakamura, K., 1986. Preparation and properties of boron nitride films by metal organic chemical vapor deposition. J. Electrochem. Soc. 133, 1120.
Nakarmi, M.L., Kim, K.H., Zhu, K., Lin, J.Y., Jiang, H.X., 2004. Transport properties of highly conductive n-type Al-rich $Al_xGa_{1-x}N$ ($x \geq 0.7$). Appl. Phys. Lett. 85, 3769.
Nakarmi, M.L., Kim, K.H., Khizar, M., Fan, Z.Y., Lin, J.Y., Jiang, H.X., 2005. Electrical and optical properties of Mg-doped $Al_{0.7}Ga_{0.3}N$ alloys. Appl. Phys. Lett. 86, 092108.
Nakarmi, M.L., Nepal, N., Ugolini, C., Al Tahtamouni, T.M., Lin, J.Y., Jiang, H.X., 2006. Correlation between optical and electrical properties of Mg-doped AlN epilayers. Appl. Phys. Lett. 89, 152120.
Nam, K.B., Li, J., Nakarmi, M.L., Lin, J.Y., Jiang, H.X., 2002. Achieving highly conductive AlGaN alloys with high Al contents. Appl. Phys. Lett. 81, 1038.
Nam, K.B., Nakarmi, M.L., Lin, J.Y., Jiang, H.X., 2005. Deep impurity transitions involving cation vacancies and complexes in AlGaN alloys. Appl. Phys. Lett. 86, 222108.
National Research Council, 2008. Radiation Source Use and Replacement: Abbreviated Version. The National Academies Press, Washington, DC. Chapter 9, https://doi.org/10.17226/11976.
Neal, J., Boatner, L., Bell, Z., Akkurt, H., McCarthy, M., 2011. Evaluation of neutron and gamma detectors for high-temperature well-logging applications. In: Future of Instrumentation International Workshop (FIIW), pp. 172–175.
Nepal, N., Nakarmi, M.L., Lin, J.Y., Jiang, H.X., 2006. Photoluminescence studies of impurity transitions in AlGaN alloys. Appl. Phys. Lett. 89, 092107.
Ngwenya, T.B., UKpong, A.M., Chetty, N., 2011. Defect states of complexes involving a vacancy on the boron site in boronitrene. Phys. Rev. B 84, 245425.
Nikolic, R.J., Conway, A.M., Heineck, D., Voss, L.F., Wang, T.F., Shao, Q., 2013. Method for Manufacturing Solid-State Thermal Neutron Detectors With Simultaneous High Thermal Neutron Detection Efficiency (> 50%) and Neutron to Gamma Discrimination (> 1.0E4). US patent 8558188.
Noonan, W.A., 2014. Neutrons: it is all in the timing—the physics of nuclear fission chains and their detection. J. Hopkins APL Tech. Dig. 32, 762.
Nose, K., Oba, H., Yoshida, T., 2006. Electric conductivity of boron nitride thin films enhanced by in situ doping of zinc. Appl. Phys. Lett. 89, 112124.
Oba, F., Togo, A., Tanaka, I., Watanabe, K., Taniguchi, T., 2010. Doping of hexagonal boron nitride via intercalation: a theoretical prediction. Phys. Rev. B 81, 075125.
Orellana, W., Chacham, H., 2001. Stability of native defects in hexagonal and cubic boron nitride. Phys. Rev. B 63, 125205.
Osberg, K., Schemm, N., Balkir, S., Brand, J.O., Hallbeck, M.S., Dowben, P.A., Hoffman, M.W., 2006. A handheld neutron-detection sensor system utilizing a new class of boron carbide diode. IEEE Sensors J. 6, 1531.
Osberghaus, O., 1950. Isotopic abundance of boron. Mass-spectrometric investigation of the electron-impact products of boron trifluoride and boron trichloride. Z. Phys. 128, 366.
Pease, R.S., 1952. An X-ray study of boron nitride. Acta Crystallogr. 5, 536.

Powers, M.J., Benjamin, M.C., Porter, L.M., Nemanich, R.J., Davis, R.F., Cuomo, J.J., Doll, G.L., Harris, S.J., 1995. Observation of a negative electron affinity for boron nitride. Appl. Phys. Lett. 67, 3912.

Rubio, A., Corkill, J.L., Cohen, M.L., 1994. Theory of graphitic boron nitride nanotubes. Phys. Rev. B 49, 5081.

Rumyantsev, S.L., Levinshtein, M.E., Jackson, A.D., Mohammmad, S.N., Harris, G.L., Spencer, M.G., Shur, M.S., 2001. In: Levinshtein, M.E., Rumyantsev, S.L., Shur, M.S. (Eds.), Properties of Advanced Semiconductor Materials GaN, AlN, InN, BN, SiC, SiGe. John Wiley & Sons Inc, New York, pp. p67–p92.

Semenoff, G.W., 1984. Condensed-matter simulation of a three-dimensional anomaly. Phys. Rev. Lett. 53, 2449.

Shakya, J., Lin, J.Y., Jiang, H.X., 2004. Time-resolved electroluminescence studies of III-nitride ultraviolet photonic-crystal light-emitting diodes. Appl. Phys. Lett. 85, 2104.

Shao, Q., Voss, L.F., Conway, A.M., Nikolic, R.J., Dar, M.A., Cheung, C.L., 2013. High aspect ratio composite structures with 48.5% thermal neutron detection efficiency. Appl. Phys. Lett. 102, 063505.

Silly, M.G., Jaffrennou, P., Barjon, J., Lauret, J.-S., Ducastelle, F., Loiseau, A., Obraztsova, E., Attal-Tretout, B., Rosencher, E., 2007. Luminescence properties of hexagonal boron nitride: cathodoluminescence and photoluminescence spectroscopy measurements. Phys. Rev. B 75, 085205.

Spieler, H.G., Haller, E.E., 1985. Assessment of present and future large-scale semiconductor detector systems. IEEE Trans. Nucl. Sci. NS-32, 419.

Stampfl, C., Van de Walle, C.G., 1998. Doping of AlxGa1 − xN. Appl. Phys. Lett. 72, 459.

Sugino, T., Tanioka, K., Kawasaki, S., Shirafuji, J., 1997. Characterization and field emission of sulfur-doped boron nitride synthesized by plasma-assisted chemical vapor deposition. Jpn. J. Appl. Phys. 36, L463.

Takahashi, T., Watanabe, S., 2001. Recent progress in CdTe and CdZnTe detectors. IEEE Trans. Nucl. Sci. 48, 950.

Uddin, M.R., Majety, S., Li, J., Lin, J.Y., Jiang, H.X., 2014a. Layer-structured hexagonal (BN)C semiconductor alloys with tunable optical and electrical properties. J. Appl. Phys. 115, 093509.

Uddin, M.R., Doan, T.C., Li, J., Ziemer, K.S., Lin, J.Y., Jiang, H.X., 2014b. Electrical transport properties of (BN)-rich hexagonal (BN)C semiconductor alloys. AIP Adv. 4, 087141.

Uddin, M.R., Li, J., Lin, J.Y., Jiang, H.X., 2017. Probing carbon impurities in hexagonal boron nitride epilayers. Appl. Phys. Lett. 110, 182107.

Uher, J., Pospisil, S., Linhart, V., Schiebar, M., 2007. Efficiency of composite boron nitride neutron detectors in comparison with helium-3 detectors. Appl. Phys. Lett. 90, 124101.

Vokhmintsev, A.S., Weinstein, I.A., 2021. Temperature effects in luminescence of associated oxygen-carbon pairs in hexagonal boron nitride under direct optical excitation within 7-1100 K range. arXiv. 2003.02789.

Vokhmintsev, A.S., Weinstein, I.A., Minin, M.G., Shalyakin, S.A., 2019. Thermally stimulated processes in the luminescence of carbon-related defects for h-BN micropowder. Radiat. Meas. 124, 35.

Wang, V., Ma, N., Mizuseki, H., Kawazoe, Y., 2012. First-principles study of intrinsic defect properties in hexagonal BN bilayer and monolayer. Solid State Commun. 152, 816.

Wang, Q.W., Uddin, M.R., Du, X.Z., Li, J., Lin, J.Y., Jiang, H.X., 2019a. Synthesis and photoluminescence properties of hexagonal BGaN alloys and quantum wells. Appl. Phys. Express 12, 011002.

Wang, Q.W., Li, J., Lin, J.Y., Jiang, H.X., 2019b. Critical thickness of hexagonal GaBN/BN heterostructures. J. Appl. Phys. 125, 205703.

Watanabe, K., Taniguchi, T., 2009. Jahn-Teller effect on exciton states in hexagonal boron nitride single crystal. Phys. Rev. B79, 193104.

Watanabe, K., Taniguchi, T., Kanda, H., 2004. Direct-bandgap properties and evidence for ultraviolet lasing of hexagonal boron nitride single crystal. Nat. Mater. 3, 404.

Watanabe, K., Taniguchi, T., Niiyama, T., Miya, K., Taniguchi, M., 2009. Far-ultraviolet plane-emission handheld device based on hexagonal boron nitride. Nat. Photonics 3, 591.

Weston, L., Wickramaratne, D., Mackoit, M., Alkauskas, A., Van de Walle, C.G., 2018. Native point defects and impurities in hexagonal boron nitride. Phys. Rev. B97, 214104.

Wirtz, L., Marini, A., Rubio, A., 2006. Excitons in boron nitride nanotubes: dimensionality effects. Phys. Rev. Lett. 96, 126104.

Yang, X., Nitta, S., Nagamatsu, K., Bae, S.Y., Lee, H.J., Liu, Y.H., Pristovsek, M., Honda, Y., Amano, H., 2018. Growth of hexagonal boron nitride on sapphire substrate by pulsed-mode metalorganic vapor phase epitaxy. J. Cryst. Growth 482, 1.

Yang, X., Nitta, S., Pristovsek, M., Liu, Y., Liao, Y., Kushimoto, M., Honda, Y., Amano, H., 2020. Scalable synthesis of multilayer h-BN on AlN by metalorganic vapor phase epitaxy: nucleation and growth mechanism. 2D Mater. 7, 015004.

Ying, J., Zhang, X.W., Yin, Z.G., Tan, H.R., Zhang, S.G., Fan, Y.M., 2011. Electrical transport properties of the Si-doped cubic boron nitride thin films prepared by *in situ* cosputtering. J. Appl. Phys. 109, 023716.

Zhu, K., Nakarmi, M.L., Kim, K.H., Lin, J.Y., Jiang, H.X., 2004. Silicon doping dependence of highly conductive n-type $Al_{0.7}Ga_{0.3}N$. Appl. Phys. Lett. 85, 4669.

Zunger, A., Katzir, A., 1975. Point defects in hexagonal boron nitride. II. Theoretical studies. Phys. Rev. 11, 2378.

Zunger, A., Katzir, A., Halperin, A., 1976. Optical properties of hexagonal boron nitride. Phys. Rev. B13, 5560.